

DEVELOPMENT AND IMPROVEMENT OF QUANTUM DOT
SENSITIZED SOLAR CELL ARCHITECTURES

By

Shawn M. Rosson

Thesis

Submitted to the Faculty of the
Graduate School of Vanderbilt University
in partial fulfillment of the requirements
for the degree of

MASTER OF SCIENCE

in

Chemistry

December, 2010

Nashville, Tennessee

Approved:

Professor Sandra J. Rosenthal

Professor David E. Cliffler

Acknowledgements

This work would not have been possible without the support of Vanderbilt University and grant 4000091167 given by Oak Ridge National Laboratory. I am grateful to my advisor Dr. Sandra J. Rosenthal and those from the Rosenthal group that contributed to my project. I would like to thank Kevin Emmitt and Dr. Nathanael Smith for their previous work on this project and their assistance in teaching me the foundations of this research. A special thanks to those who acquired data that was used for my project, specifically Dr. Michael Schreuder, Melissa Harrison, and Amy Ng. I would also like to thank Dr. James McBride, Dr. Michael Schreuder, and Albert Dukes for their helpful discussions and guidance in areas where I was not as knowledgeable. I am appreciative of the time and effort that Dr. Anthony Hmelo put into my research through instrument training and support. I began graduate school with no research background, and with their help, I learned to apply my knowledge and critical thinking to real problems to find innovative solutions. I enjoyed my time learning many new techniques, instruments, and concepts under the guidance of these great people.

Table of Contents

	Page
Acknowledgements.....	iii
List of Tables	vii
List of Figures	viii
Chapter	
I. INTRODUCTION	
1.1 Background.....	1
1.2 Nanostructured Substrates	3
1.2.1 TiO ₂ Nanotube Arrays.....	4
1.2.2 ZnO Nanorod Arrays.....	6
1.3 Semiconductor Nanocrystals	7
1.3.1 Light Absorbing Properties for Photovoltaics.....	7
1.3.2 Quantum Confinement Effects.....	8
1.3.3 Marcus Theory	10
1.3.4 Ligand Effects	12
1.4 Electrolyte.....	14
1.5 IV Curves for Solar Cell Characterization.....	16
1.5.1 Short Circuit Current.....	17
1.5.2 Open Circuit Voltage	21
1.5.3 Fill Factor	22

1.5.4 Efficiency Measurement and Calculation	23
II. EXPERIMENTAL	
2.1 Nanostructured Substrate Fabrication	25
2.1.1 TiO ₂ Nanotube Fabrication.....	25
2.1.2 Free-standing Nanotube Array Fabrication.....	28
2.1.3 ZnO Fabrication	31
2.2 Nanocrystal Synthesis and Modification	32
2.2.1 Nanocrystal Synthesis	32
2.2.2 Ligand Exchange.....	35
2.3 Deposition Methods	37
2.3.1 Immersion Coating.....	38
2.3.2 Electrophoretic Deposition.....	39
2.4 Device Preparation.....	41
2.4.1 Indium-Tin Oxide Electrode Modification.....	41
2.4.2 Polymer Deposition.....	41
2.4.2 Sealing the Electrolyte Device	42
III. CHARACTERIZATION TECHNIQUES FOR SOLAR CELL MATERIALS	
3.1 Scanning Electron Microscopy.....	43
3.2 Rutherford Backscattering Spectroscopy (RBS)	44
3.3 Solar Simulation Testing.....	50
IV. CONCLUSIONS AND FUTURE DIRECTIONS	
4.1 Conclusions.....	54
4.2 Future Directions	55

4.2.1 Graphene Counter-electrode.....	55
4.2.2 Solid-state Photovoltaic Device using Free-standing Nanotubes	55
4.2.3 ZnO Solid-state Device	56
4.2.4 UV-Vis Study on Free-standing Nanotubes.....	57
Appendix	
A. OAK RIDGE POLYMER EXCHANGE EXPERIMENT	
A.1 Introduction.....	58
A.2 Ligand Exchange.....	60
A.3 Characterization	61
B. TiO ₂ NANOTUBE IMPRINTING	
B.1 Introduction	64
B.2 Characterization	64
C. PRELIMINARY UV-VIS STUDY ON NANOCRYSTAL-COATED FREE- STANDING NANOTUBES	
C.1 Introduction	65
C.2 Characterization	65
REFERENCES	67

List of Tables

Table	Page
3.1 RBS constants and variables.....	49
A.1 Ligand names and structures.....	59

List of Figures

Figure	Page
1.1 Grätzel cell diagram	2
1.2 Solid-state quantum dot sensitized solar cell architecture	3
1.3 Pore formation process	5
1.4 Crystal structure of rutile and anatase TiO ₂	6
1.5 Solar radiation reference spectrum	9
1.6 Potential energy and activation energy diagrams (Marcus Theory)	10
1.7 Thiol band alignment with CdSe and CdTe nanocrystals	14
1.8 Factors affecting short-circuit current	18
1.9 Charge transport diagram for TiO ₂ with nanocrystals	20
1.10 V _{OC} explanation diagram	22
1.11 Effect of shunt and series resistance on fill factors	23
1.12 Effect of temperature and light intensity on IV curves	24
2.1 Diagram of the Teflon etch cell for anodization	25
2.2 Current vs time curve from anodization	26

2.3 SEM images of TiO ₂ nanotubes.....	27
2.4 Free-standing nanotube fabrication process.....	29
2.5 SEM images of free-standing TiO ₂ nanotubes.....	30
2.6 Image of free-standing nanotubes with evaporated aluminum.....	31
2.7 SEM image of ZnO nanorods	32
2.8 Nanocrystal synthesis setup	33
2.9 CdSe nanocrystal illustration after ligand exchange.....	35
2.10 Chemical linking diagram.....	37
2.11 SEM of aggregated nanocrystals on TiO ₂ nanotubes	38
2.12 EPD setup.....	40
3.1 SEM images of TiO ₂ nanotube cracking and surface debris	44
3.2 RBS instrument diagram.....	45
3.3 RBS spectrum of bismuth standard.....	46
3.4 Pictures of the solar simulation setup	50
3.5 IV curves for a solid-state solar cell (dark and light).....	51
3.6 IV and PV curves for two electrolyte-based TiO ₂ nanotube solar cells	52
3.7 IV curve for an electrolyte-based ZnO nanorod solar cell.....	53

4.1 Device structure for a free-standing nanotube-based device	56
4.2 Device structure for a ZnO nanorod-based device	57
A.1 RBS spectrum of CdSe nanocrystals before ligand exchange	63
A.2 RBS spectrum of CdSe nanocrystals after ligand exchange	63
B.1 SEM images of imprinted nanotube arrays	64
C.1 UV-Vis spectra for nanocrystals & TiO ₂ nanotubes with & without nanocrystals.....	66

Chapter 1

Introduction

1.1 Background

As the drive to seek alternative energy sources significantly increases across the world, there is a growing interest in low-cost, easily manufactured, and efficient energy sources. One of those sources is the harnessing of the sun's energy through the excitation of semiconductor materials. This technology has been around since 1839 with the discovery of the photovoltaic effect by Alexandre Edmond Becquerel.^[1] The photoelectric effect was first applied to a device in 1883 by Charles Fritts with the development of a selenium and gold *pn* junction device with approximately 1 % efficiency.^[2] The first p-n junction solar cell design was published by Bell Laboratories in 1954 with an efficiency of 6 %.^[3] The innovation by Bell Labs produced the first viable commercial solar cell, which revolutionized the photovoltaic industry. Since then, improvements have been made to give photovoltaics more accessibility in the global energy market. The most efficient devices are currently achieving at least 43 % photoconversion efficiency.^[4] These types of solar cells are very expensive and combine several devices into one solar cell along with the concentration of incoming light to achieve the high efficiency. Lower-cost, more easily manufactured devices have also been developed at the expense of photoconversion efficiency. In 1991, Grätzel

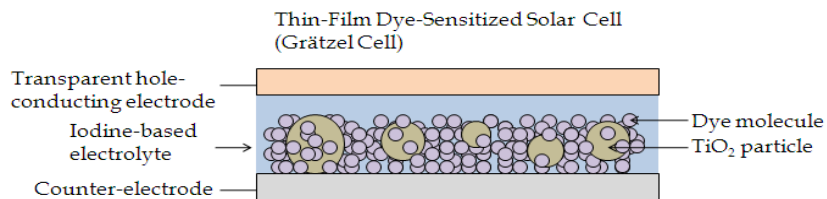


Figure 1.1: Grätzel cell depicted in a side view cartoon

published his research on the first dye-sensitized solar cell ^[5] which demonstrated an efficiency of 7.1-7.9 %. This device structure is shown in Figure 1.1. This work is being advanced by moving toward more structured substrates and better materials for light harvesting.

The solid-state device architecture I have been working with is shown in Figure 1.2. It shows a nanostructured TiO₂ array coated with semiconductor nanocrystals and filled with a hole-conducting material. The bottom electrode is titanium and the top electrode is indium-tin oxide (ITO) coated glass. I have also been working with a device of similar architecture with the hole-conducting polymer replaced with a liquid electrolyte to compare the results of the solid-state device to the redox-electrolyte based devices. This work was done as an effort to improve the weaknesses of the Grätzel cell, such as limited surface area, poor charge transportation, and less than ideal light harvesting that contribute to a limited maximum efficiency.

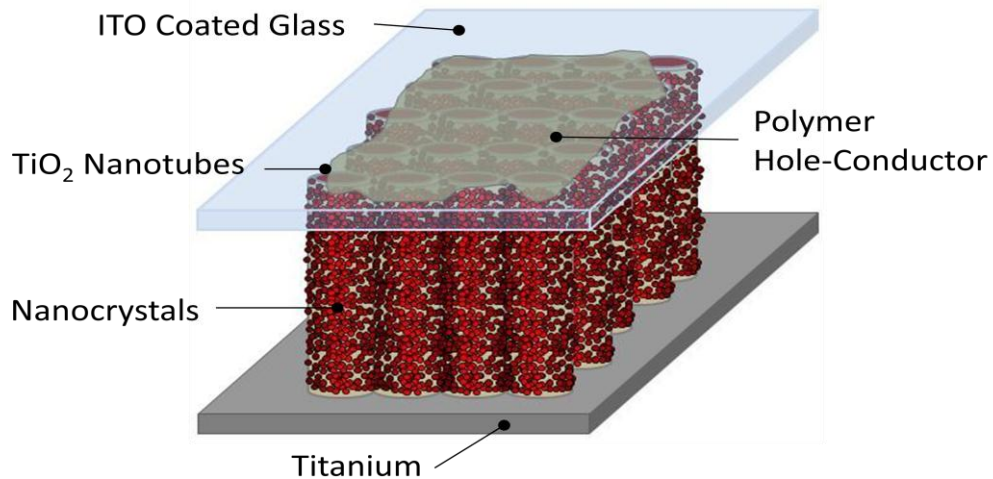


Figure 1.2: Cartoon depicting the device structure of a solid-state quantum dot-sensitized solar cell with a TiO₂ nanotube substrate.

1.2 Nanostructured Substrates

A large amount of research in this project has been dedicated to improving the Grätzel cell structure. The limitations inherent to the dye-sensitized solar cell (DSC) design can be overcome by providing more order and better charge transport. One solution to this problem is to move from a TiO₂ mesoporous matrix to an ordered array of nanostructures.

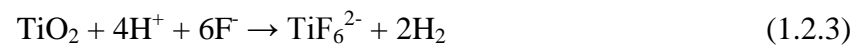
Photovoltaic devices will always be limited by recombination within the device materials. In thin-film devices, the distance the charges have to travel within the electron transport material to be collected at the electrode limits the maximum film thickness because recombination is increased by the multidirectional matrix of particles. Through the separation of charges into different materials over a short period of time, recombination is greatly reduced. ^[6] Using ordered nanostructures as a substrate as

compared to planar films demonstrates the ability to shuttle charges more efficiently over a longer distance. Unidirectional charge transport within a single material cannot be achieved in thin-film devices without ordered structures. TiO₂ nanotubes and ZnO nanorods have received attention as substrates for photovoltaic devices because of their ability to increase the surface area while providing better charge transport. These structures are easily processable under normal lab conditions and are fairly low-cost.

Also, the quantity of light harvesting molecules that contribute to overall device efficiency can only be improved by increasing the surface area of the substrate that the donor material can be sensitized to. With the limits on thin-film thickness due to recombination, another device structure must be used to achieve increased surface area. Both the TiO₂ and ZnO nanostructures accomplish this increase in surface area.

1.2.1 TiO₂ Nanotube Arrays

TiO₂ nanotubes are fabricated through a simultaneous multi-step anodization process involving the formation of TiO₂, oxidation of the titanium metal, and dissolution of the barrier layer as described by the following chemical equations: ^[7]



Pore formation begins with a natural oxide barrier layer. A reaction of the fluoride ion with the TiO_2 barrier layer creates pits that eventually become the inside pores of the nanotubes. As the dissolution of the barrier layer occurs, there is an increased field at the bottom of the pores that leads to oxide growth. The chemical dissolution and barrier growth occur at a slower rate as the tube length increases, resulting in slowed tube growth as time progresses.

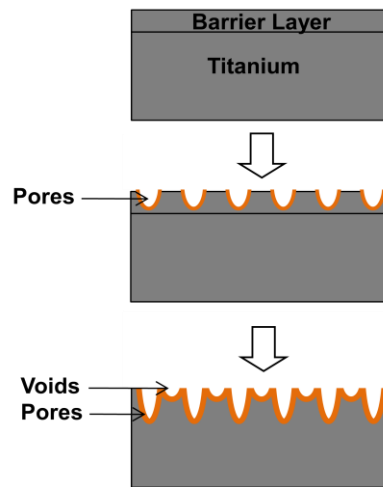


Figure 1.3: Schematic showing pore formation that leads to nanotube growth. ^[8]

The diameter and length of the tubes can be altered by varying the parameters of the anodization. Fluoride concentration in the electrolyte, the potential applied across the electrodes, and the duration that the potential is applied all have an effect on the morphology of the nanotubes. Increasing fluoride concentration in the electrolyte creates longer tube lengths in a shorter time at the expense of quality. Higher anodization

potentials result in longer tube lengths as well as increased inner and outer tube diameters. ^[9]

The anodization process results in well-ordered, vertically aligned nanotubes with an amorphous crystal structure. Amorphous TiO_2 has no defined crystal structure, and is not suitable for photovoltaics. Amorphous nanotubes are insulating, and they must be annealed to convert the crystal structure to the anatase form for use in a device. By doing so, the nanotubes become electron conducting. After the annealing step, the nanotube walls are anatase and are separated from the titanium base by a small rutile layer. ^[10, 11]

The crystal structures of rutile and anatase TiO_2 are given in Figure 1.4.

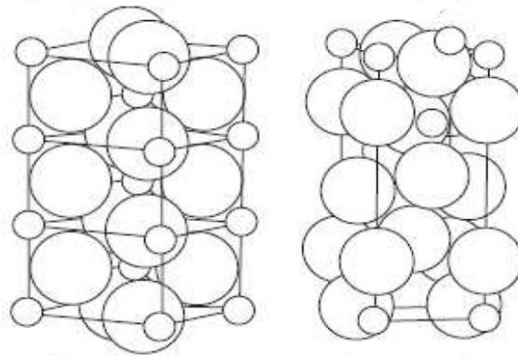


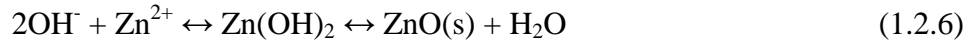
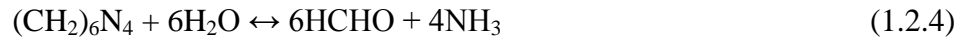
Figure 1.4: Crystal structure of rutile (left) and anatase (right) TiO_2

1.2.2 ZnO Nanorod Arrays

TiO_2 is sufficient as a material for photovoltaic devices although the structure of nanotubes has been found to be a problem because of the difficulty of filling the tubes. A nanorod structure accomplishes the same increase in surface area, but it is easier to fill around rods than to pack material into tubes. The band gap of ZnO (3.3 eV) is very close

to that of TiO₂ (3.2 eV), making it a viable replacement for TiO₂ without changing the band alignment of the materials significantly. ^[12]

ZnO nanorods are fabricated through a chemical bath deposition technique, using a seed layer deposited through a spin-cast technique. There are a variety of precursor materials and methods for creating ZnO nanorods, ^[13, 14, 39] although it has been shown that a seed layer generally makes more ordered and better quality structures. Chemical bath deposition was chosen because of the ease of fabrication. The main chemical process in this CBD method is described by the following equations: ^[13]



1.3 Semiconductor Nanocrystals

1.3.1 Light Absorbing Properties for Photovoltaics

Another deviation from the DSC design is the use of different light harvesting agents. Semiconductor nanocrystals have been used ^[15, 16] as a replacement for the ruthenium-based dyes in Grätzel-style DSCs. Using nanocrystals as light harvesters has many benefits over ruthenium-based dyes. Nanocrystals are better light absorbers, as

demonstrated by their higher molar extinction coefficients, approximately $10^5 \text{ cm}^{-1}\text{M}^{-1}$ and $10^6 \text{ cm}^{-1}\text{M}^{-1}$ for CdSe^[17] and PbSe respectively^[18] while dyes^[19] have extinction coefficients around $10^3 \text{ cm}^{-1}\text{M}^{-1}$. Their absorption can also be optimized by varying the size during growth of the nanocrystal, unlike dyes. This provides the opportunity to tune the size of the nanocrystal so that it absorbs the maximum amount of the solar spectrum, which is more difficult than with dyes.

1.3.2 Quantum Confinement Effects

Semiconductor nanocrystals, also referred to as quantum dots, are crystalline semiconductors with a diameter between approximately 2-10 nm. At this size, quantum effects are evident as a result of the nanocrystal radius being smaller than the exciton Bohr radius. The Bohr exciton radius is the average distance an electron will be from a hole when an exciton is created. In CdSe, the Bohr radius is 5.4 nm.^[20] When the size of a CdSe nanocrystal is reduced below a 5.4 nm radius, energy levels are no longer continuous and become split into discrete energy levels. This quantum confinement phenomenon results in size tunable absorption and emission properties, which can be taken advantage of in many applications such as solid-state lighting, biological labeling, and most importantly for this project, photovoltaics.

The quantum confinement-induced size-tunable properties are very useful in photovoltaics. It eliminates the need to synthesize difficult organic molecules to get the correct band-alignment with the acceptor material. Size dependent absorption allows the

selection of an ideal size based on the amount of the solar spectrum that can be absorbed while also considering charge transfer from the nanocrystal to the acceptor material. Larger nanocrystals will absorb more of the solar spectrum, but may not transfer the generated charges efficiently to the acceptor material. The charge transfer rate depends on the band alignment of the two materials, ^[15] which changes as the size of the nanocrystal varies. Kongkanand *et al.* ^[21] report that the injection rate of an electron is dependent on the difference in the nanocrystal conduction band and the conduction band of the electron conducting material. This concept is covered in more detail under the explanation of open circuit voltage.

Figure 1.5 shows the reference spectrum for solar radiation. As can be seen from the spectrum, the sun emits electromagnetic radiation to about 300 to 2500 nm. This means that the ideal light harvester will absorb to 2500 nm and contribute the generated charges to the photoconversion efficiency effectively.

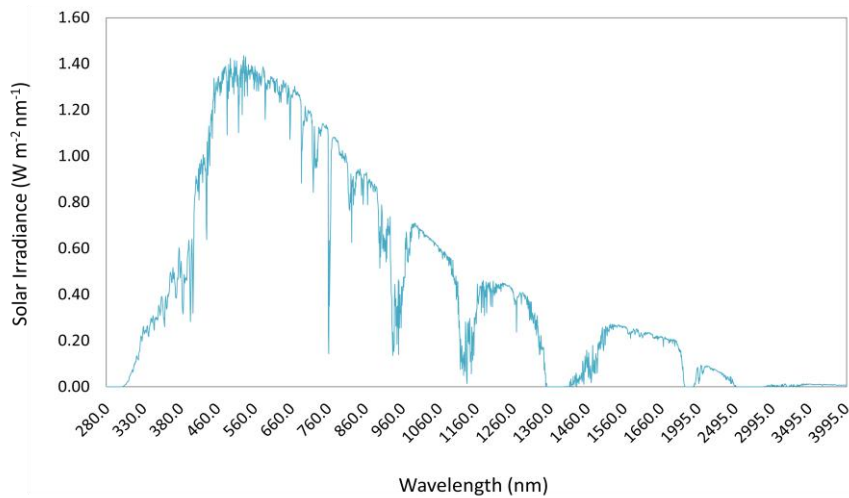


Figure 1.5: ASTM G173-03 Reference Spectrum. ^[22]

1.3.3 Marcus Theory

Marcus theory can be applied to this system to describe the charge transfer kinetics of the system. ^[23, 24] In a model with two molecules in a solvent system, the potential energy surface of the two molecules in their initial state and the potential energy surface of the products after charge transfer are plotted with an x and y-axis representing reaction coordinate and energy respectively.

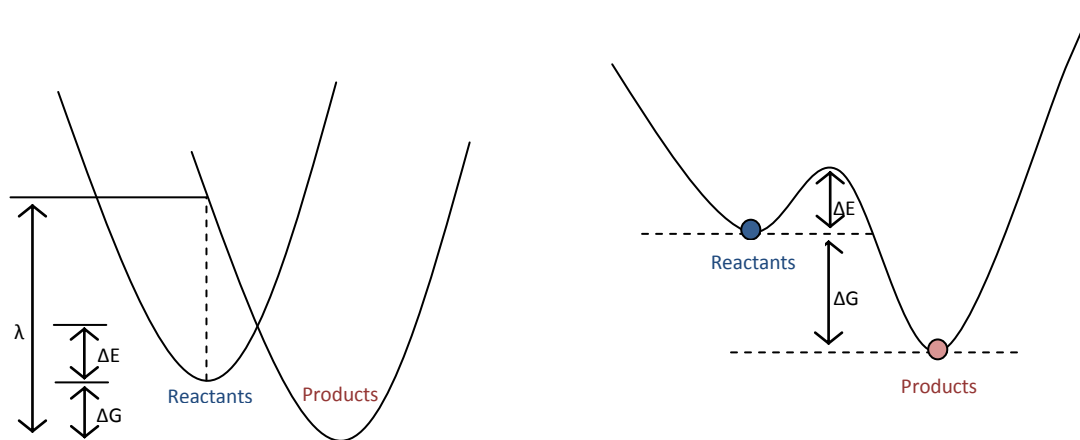


Figure 1.6: Nuclear potential-energy curves (left) and an activation energy diagram (right) for a generic reaction.

Marcus modified the Arrhenius Equation, resulting in the following equation:

$$k_{\text{et}} = \frac{2\pi}{\hbar} |H_{AB}|^2 \frac{1}{\sqrt{4\pi\lambda RT}} \exp\left(-\frac{(\lambda + \Delta E^0)^2}{4\lambda RT}\right) \quad (1.3.1)$$

$$\lambda = \lambda_i + \lambda_o \quad (1.3.2)$$

where H_{AB} is the electronic matrix element describing the electronic coupling of the reactants' electronic state with the products, ΔE^0 is the energy (enthalpy) of reaction at a separation distance r in the system, λ_i is the change in bond lengths of the reactants, and λ_o is the change in solvent orientation coordinates.

Factors such as solvent effects, distance between the molecules, and size of the molecule determine the charge transfer kinetics. In our system, these effects must be considered as a whole to find the most favorable nanocrystal materials and sizes. Solvent effects play a larger role with smaller nanocrystals, which are more highly solvated than larger nanocrystals, affecting the λ_o term more for smaller nanocrystals. After electron transfer from the nanocrystal to the electron conductor, the solvent molecules must immediately adjust to the new electronic arrangement, creating a high-energy state ^[23]. This implies that more solvent around the nanocrystal would result in a slower charge transfer due to an increased ΔE , as seen in the nuclear potential-energy curve diagram in Figure 1.6. In a solid-state device, there would not be any solvent interactions. Electron tunneling in this system would mainly be affected by the distance between the molecules and the nanocrystal band gap, which is determined by the size of the nanocrystal.

H_{AB} from Equation 1.3.1 is affected by the distance between the nanocrystal and the electron acceptor. Since H_{AB} is squared, it has a significant effect on k_{et} and shows that distance is an important factor to consider. ΔE^0 , also from Equation 1.3.1, gives the energy required, or enthalpy of the reaction, to rearrange the system after charge transfer at a certain defined distance between the nanocrystal and the acceptor. In a solvent free system, such as a solid-state device, ΔS^0 in that system can be assumed to be approximately zero ^[24]. Therefore, $\Delta E^0 (\approx \Delta G^0 + T\Delta S^0) \approx \Delta G^0$. Since the enthalpy of the

reaction, ΔE^0 , and the free energy, ΔG^0 are approximately equal, ΔG^0 can be substituted into Equation 1.3.1. The difference between the nanocrystal and electron acceptor conduction bands determines the value of $-\Delta G^0$, the driving force. As the driving force increases with decreasing nanocrystal size, the charge transfer rate increases, with a maximum value when the driving force equals the reorganization energy ^[15]. In this way, nanocrystal size also affects the charge transfer rate.

For any specific nanocrystal type, nanocrystal size and ligand length can be varied to experimentally determine the optimal charge transfer for any solid-state system. However, if the theory behind the charge transfer kinetics can be understood, less experimental data will be needed to determine the optimal materials and ligands for each potential system. The theory also provides an explanation as to why choosing a nanocrystal size or composition based on absorption or charge transfer alone is misguided. The system must be optimized by considering how changing one parameter will affect the rest of the system.

1.3.4 Ligand Effects

In discussing charge transfer kinetics, the distance between the nanocrystal and other materials is important. Electron tunneling happens at short distances, and bulky ligands increase that distance, thus decreasing the probability of tunneling ^[25]. Bulky, long alkyl-chain ligands also insulate the nanocrystal, which affects the transfer kinetics as well. The ligands on the as-synthesized nanocrystals can be exchanged for various

other ligands to achieve more desirable binding or electrical properties. In our device structure, we must find a ligand that binds well to the nanocrystal and the substrate as a means of attaching them. Sulfur has been found to form a strong bond to Cd, so one end of the ligand can be functionalized with a thiol group. On the other end, the group must bind well to TiO₂. Carboxylic groups have been found to bind well to TiO₂, so it is chosen to be the other end group. One further consideration in determining the optimal ligand is the length of the carbon chain between the end groups and whether there should be additional substituents that encourage charge transfer between the donor and acceptor material.

Sulfur binds tightly to Cd; therefore it easily replaces the more loosely bound ligands that exist on the as-synthesized nanocrystals.^[26] It has been shown to replace amines, but it does not easily remove phosphonic acids, alkyl phosphine oxides, or trioctylphosphine (TOP).^[26-28] Attaching thiols to nanocrystals has an effect on the photoluminescence properties, usually resulting in complete quenching in CdSe nanocrystals.

Wuister *et al.*^[29] find that thiol ligands enhance the quantum efficiency in CdTe nanocrystals while almost completely quenching emission in CdSe nanocrystals. They conclude that this is a result of the redox energy level of the thiol being above the valence band of the CdSe nanocrystal, making it energetically favorable for the hole to move to the thiol. The hole-trapping in the thiol increases the rate of the non-radiative decay process, which quenches photoluminescence. In CdTe, it is not energetically favorable for the hole to move to the thiol since the redox energy level is below the valence band.

Hole-trapping in CdSe may have a negative effect on the efficiency by reducing the chance that the hole will leave the nanocrystal before it recombines. In this way, the efficiency may be limited by the effect of the thiol ligand on CdSe. This explanation also shows that the effect of thiols on nanocrystals is not universal. Therefore, the use of CdTe and other nanocrystal compositions will have differing results. Despite the hole-trapping nature of the thiol with CdSe, it is still commonly used as a chemical linker [14, 30, 31]

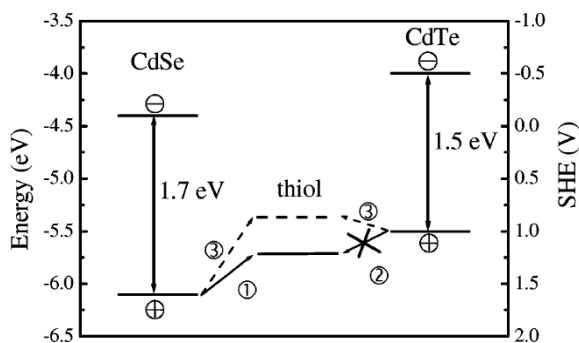


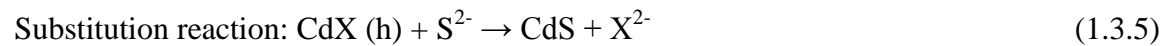
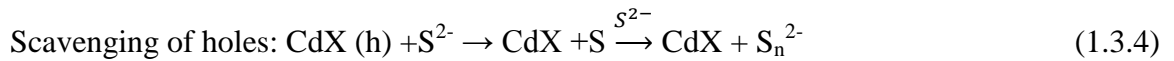
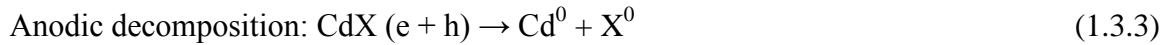
Figure 1.7: Band alignment of CdSe and CdTe nanocrystals with respect to vacuum (left scale) and a standard hydrogen electrode (right scale). Hole trapping quenches emission in CdSe (process 1) and both CdSe and CdTe (process 3). Process 2 does not result in hole-trapping in CdTe. The dotted and solid lines between CdSe and CdTe are energy levels for different thiols. [29]

1.4 Electrolyte

This project was initially designed to produce an all-solid-state solar cell. However, due to very low efficiencies of the solid-state devices and the lack of previously published, efficient devices of similar architecture within our group to compare to literature, we attempted to make some devices with the standard electrolyte device structure as a comparison. [5, 32-35] This structure makes use of a redox electrolyte

that scavenges holes from the nanocrystals by oxidizing and contributing those charges to the electrode through reduction.

A redox electrolyte is used in many published device structures. In many of Grätzel's publications, ^[5, 32, 33] an I_3^-/I^- electrolyte is used. This redox couple is compatible with the ruthenium-based dyes that are used in those DSCs. An iodide electrolyte, however, is not compatible with a nanocrystal system. Over time, it will degrade the nanocrystals, causing decreased device performance. The S^{2-}/S_n^{2-} is a redox couple that provides the most stability in a nanocrystal-based device. ^[34, 35] There are limitations in nanocrystal materials that can be used with a sulfide electrolyte as well. NaS stabilizes CdSe and CdS nanocrystals, but has been shown to degrade CdTe nanocrystal devices. The reactions involved at the interfacial region between the nanocrystal and the electrolyte are as follows: ^[36]



The reaction that occurs in the CdTe system forms a barrier sulfide layer that affects the performance of the device, resulting in faster emission decay in the presence of NaS electrolyte as compared to in air. Emission decay has been shown to be improved in the presence of NaS as compared to that in air for CdSe nanocrystals, which is why I have chosen this as the electrolyte for my device architecture.

When using an electrolyte system, the counter-electrode has a significant effect on the device's ability to function properly. An electrocatalytic material, such as platinum or graphite, must be used as a counter-electrode or the efficiency will remain extremely low. A platinized electrode is often used in device structures because of its ability to catalyze the redox reaction in iodide electrolytes without being consumed or changed in the reaction. Platinum, although commonly used with polysulfide electrolytes, has been shown to have much higher series resistance using polysulfide electrolytes than with iodide electrolytes. It has been suggested that sulfur in the polysulfide electrolyte attaches to the platinum, which causes this increased series resistance.^[31] A more ideal electrocatalytic material for this system, according to electrode studies using polysulfide electrolytes,^[37, 38] is CoS.

Nanocrystal devices have generally performed lower than their dye counterparts possibly because of the continued use of platinum as an electrode when it has been demonstrated that platinum is not ideal for a NaS electrolyte. A replacement of platinum would not only decrease the cost of the device materials, but it may also increase the efficiency of quantum dot sensitized solar cells, making them comparable to dye-sensitized solar cells.

1.5 IV Curves for Solar Cell Characterization

The components of different devices and different device architectures have been discussed. Once these devices have been fabricated, they are characterized by measuring

their output under illumination. We use a standard method for measuring solar cell performance. This method involves a potential scan from one voltage to another while measuring the resulting current through the device under dark and light conditions. The current-voltage (IV) curve produced by the potential scan gives important information about what is going on in the device. The shape of the IV curve tells if the device is working properly and if there are any efficiency losses that can be corrected. Short circuit current (I_{SC}) and open circuit voltage (V_{OC}) are two values of importance given in the IV curve. They indicate the maximum current and voltage, respectively, in the area of interest. These values are used to calculate the fill factor and will be discussed in more detail in this section. Analysis of an IV curve ultimately gives the I_{SC} , V_{OC} , fill factor (FF), and efficiency (η).

1.5.1 Short Circuit Current

The I_{SC} value, often written J_{SC} to account for the current within a certain measured area, is the amount of current within the device when there is no potential applied, so it is found as the x-intercept of an IV curve. From now on, short-circuit current density (J_{SC}) will be used instead of I_{SC} to describe the current in the device. V_{OC} appears as the y-intercept and gives the voltage where there is no current flowing through the device. J_{SC} is more easily improved than V_{OC} to achieve a higher efficiency. Therefore, more effort has been focused on improvement in this area. Short circuit current involves four major contributions that affect its magnitude, ^[39] 1) absorption

efficiency, ²exciton diffusion, ³charge transfer, and ⁴collection of charges at the contacts as shown in Figure 1.8.

The first step is affected by the molar absorptivity and band gap of the light harvester as well as the concentration of light absorbers contributing to the current within the device. Absorption strength is measured with UV-Vis spectroscopy and is calculated according to the Beer-Lambert law, which is $A = \epsilon bc$. A is the absorption intensity in arbitrary units (a.u.), ϵ is molar absorptivity measured in $M^{-1}cm^{-1}$, b is the length of the cuvette parallel to the beam measured in cm, and c is the concentration of the solution measured in M. Transitioning from a material with a higher molar absorptivity should be accompanied by an increase in J_{SC} . The band gap of the absorber is important as well, as it determines the amount of the solar spectrum that can be absorbed. A larger nanocrystal will absorb more of the solar spectrum than a smaller diameter nanocrystal, therefore giving it the ability to create excited electrons at higher wavelengths. This gives larger nanocrystals the ability to use more of the spectrum to convert light into excited electrons, thus contributing more charges to the overall current.

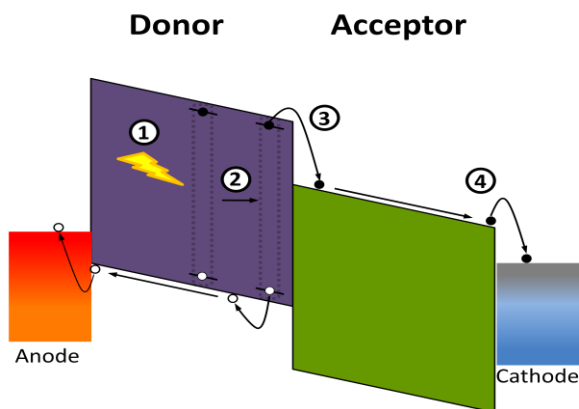


Figure 1.8: Diagram of the factors affecting short circuit current within a bulk heterojunction device with a donor/acceptor interface. The four factors are (1) absorption (2) diffusion (3) charge transfer (4) charge collection. ^[39]

The concentration of nanocrystals in the device is a significant factor to consider. Short circuit current increases proportional to the concentration of nanocrystals assuming the thickness does not exceed the exciton diffusion length by a significant amount. In thin film devices, only certain thicknesses can be achieved without diminished contribution from thicknesses beyond that point. Leschkies *et al.* ^[40] have reported that approximately 100 nm film thickness is the limit for quantum dot thin films, beyond which recombination occurs before the charges can be collected. This is the reasoning behind nanostructured substrates, which increase the donor/acceptor interface surface area and allows for more quantum dots to contribute to the current without recombination being as much of a factor.

The second step involves exciton diffusion from the area of the initial excitation to the donor/acceptor interface. The time an exciton takes to reach the donor/acceptor interface affects recombination rates within the absorber. Faster diffusion rates result in fewer losses due to recombination. This is mostly influenced by the size and material composition of the absorber.

The third step involves the transfer of charges from the donor to the acceptor at the interface. As the charges build up at the interface, the exciton dissociates and electrons are transferred to the acceptor material. As described earlier, Marcus theory ^[23] can be used to understand the mechanics of the charge transfer process between materials. Charge transfer in our system is driven by a photoinduced chemical potential energy gradient as well as an electrical potential energy gradient. According to Gregg ^[16] the photoinduced chemical potential gradient cannot be ignored to fully understand this

system although most literature focuses on the electrical potential gradient as the driving force.

Nanocrystal ligands must also be considered when dealing with charge transfer. Short chain ligands are preferred to ensure close contact between the donor and acceptor. [25, 37, 38] This is a result of the tunneling probability of the charges and the insulating nature of long alkyl chain molecules. Short distances increase the probability for tunneling to occur, as compared to long distances which inhibit tunneling altogether. Bakkers *et al.* [25] have studied CdSe QDs chemisorbed to a Au substrate using various dithiol linking molecules and concluded that the tunneling rates are exponentially decreased as distance increases.

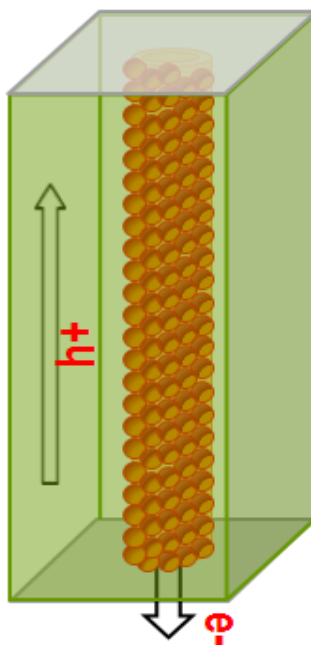


Figure 1.9: Diagram of charge transport within a nanotube-based device.

The fourth step involves charge collection at the electrodes. Figure 1.9 shows the transport pathways in a standard nanotube based device. Electrons are transported within the tubes to the bottom electrode, while the holes are transported to the top electrode through the electrolyte or solid-state hole conducting material. Once the charges reach the electrode, the charges are transferred to the electrode and contribute to the overall current of the device.

1.5.2 Open Circuit Voltage

In devices similar to our solid-state device structure, V_{OC} is affected by the built in potential, which is determined by the mismatch of work-functions of the cathode (ϕ_{Ca}) and anode (ϕ_{An}) and also by the donor/acceptor band alignment. Mihailitchi *et al.* ^[41] showed that for non-ohmic contacts, V_{OC} is determined almost solely by $\phi_{Ca} - \phi_{An}$, while for ohmic contacts it is dependent on the difference in HOMO and LUMO levels in the acceptor and donor, respectively, as shown in Figure 1.10. Liu *et al.* ^[42] have shown that solvent-induced morphology effects can also significantly influence V_{OC} in polymer bulk-heterojunction devices.

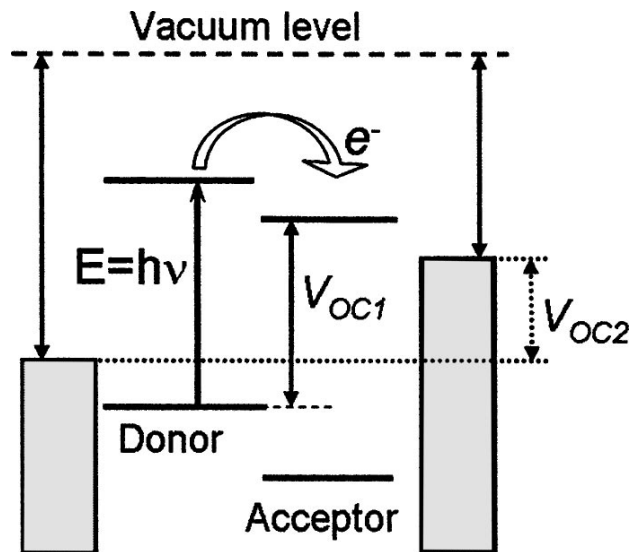


Figure 1.10: Schematic showing the maximum and minimum V_{OC} value, V_{OC1} and V_{OC2} respectively, in a donor/acceptor BHJ solar cell. ^[41]

1.5.3 Fill Factor

Even with good J_{SC} and V_{OC} values, the photoconversion efficiency may still be low due to a poor fill factor (FF). The FF reveals how well a device performs compared to its maximum theoretical power output, which is indicated on an IV curve of a solar cell by the “squareness” of the curve. FFs are calculated using the following equation:

$$FF = \frac{J_{Max} * V_{Max}}{J_{SC} * V_{OC}} \quad 1.5.1$$

where J_{max} is the current density associated with the maximum power, V_{max} is the voltage associated with the maximum power, and J_{SC} and V_{OC} have been previously defined.

FFs values are affected by two factors, series and shunt resistance. Series resistance arises as a result of the individual resistances in the materials used in a device. Shunt resistance results from leakage of current within the device due to poor transport pathways that increase recombination and contacts of different polarity. [2] For the best possible FF, series resistance should be low and shunt resistance should be high.

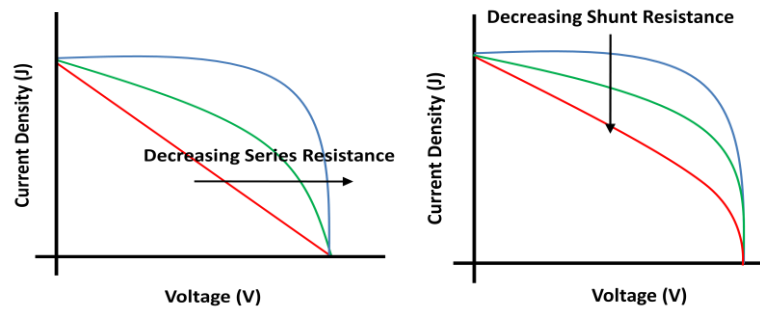


Figure 1.11: IV curves showing the effect of series resistance (left) and shunt resistance (right) on the fill factor of a solar cell. The colors indicate the quality of the fill factors, in order from blue to red in decreasing quality.

1.5.4 Efficiency Measurement and Calculation

Efficiencies are calculated using the data points generated in the IV curve. First, all of the current data is multiplied by its corresponding voltage giving power, according to the equation $P = IV$. The maximum power value is then used to calculate the efficiency using the following equation:

$$\eta = \frac{P_{\max}}{P_{in}} * 100 \% = \frac{J_{SC} * V_{OC} * FF * A_{pm}}{I_0} * 100 \% \quad 1.5.2$$

where η is efficiency, P_{\max} is the maximum power, P_{in} is the incoming power, A_{pm} is the area of the power meter used to measure the incoming light intensity, I_0 is the incoming light intensity, and J_{SC} , V_{OC} , and FF have already been defined.

Efficiencies are reported as a percentage of power produced based on the amount of input power. It is important that the reported efficiencies are comparable to other published devices. For this reason, every device must be tested experimentally in a standard way to ensure consistency in measurements, and certain factors such as temperature and light intensity must be considered.^[43] Variations in temperature and light intensity have a large effect on the output of a device. Temperature variations affect the V_{OC} while maintaining a constant J_{SC} . Lower temperatures result in increased V_{OC} values. Light intensity has an effect on the J_{SC} due to increased current generation. The V_{OC} is not affected greatly by increased light intensity. These factors are displayed in Figure 1.12.

Due to these variations in power output, the standards referred to as standard test conditions (STC) have been set by the photovoltaic industry. It includes a temperature of 25°C and an irradiance of 1000 W/m^2 with an air mass 1.5 (AM 1.5) spectrum.

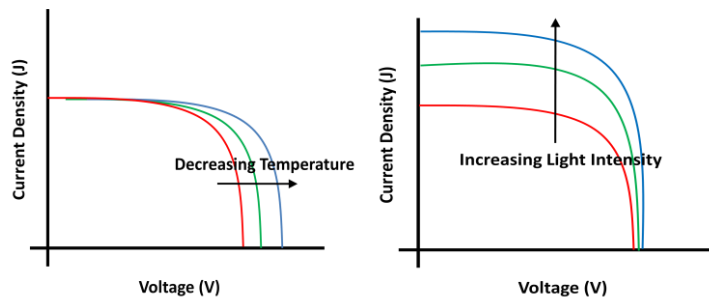


Figure 1.12: Temperature and light intensity effects on the IV curve of a photovoltaic device.

Chapter 2

Experimental and Results

2.1 Nanostructured Substrate Fabrication

2.1.1 TiO₂ Nanotube Fabrication

Nanotube arrays are created on a cleaned 2 cm x 2 cm x 0.25 mm titanium foil (99.7 % pure from Sigma Aldrich) using a fluoride containing electrolyte, platinum counter-electrode, and a machined Teflon etch cell shown in Figure 2.1.

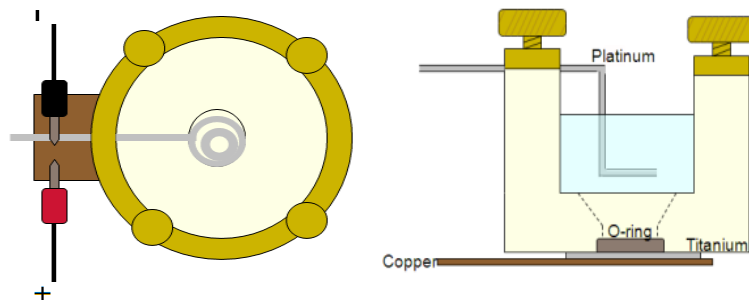


Figure 2.1: Teflon etch cell used for anodization and electrophoretic deposition

The fluoride-based electrolyte consists of 0.3 % NH_4F and 1 % H_2O dissolved in ethylene glycol. The solution is pre-anodized ^[43] by applying 60 V through the electrolyte in a beaker using two platinum electrodes over 24 h.

Anodization of the titanium foils to form nanotubes requires an applied potential and a fluoride containing electrolyte. In this work the voltage was set to 60-80 V over 5-48 h using an electrolyte containing 0.2-0.3 % NH_4F . The parameters were changed depending on the desired morphology of the tubes. After the anodization process is complete, the electrolyte is pipetted out, and the etch cell is rinsed with ethanol. The resulting nanotube array is sonicated in ethanol for 5 minutes to remove any residue left on the surface of the tubes.

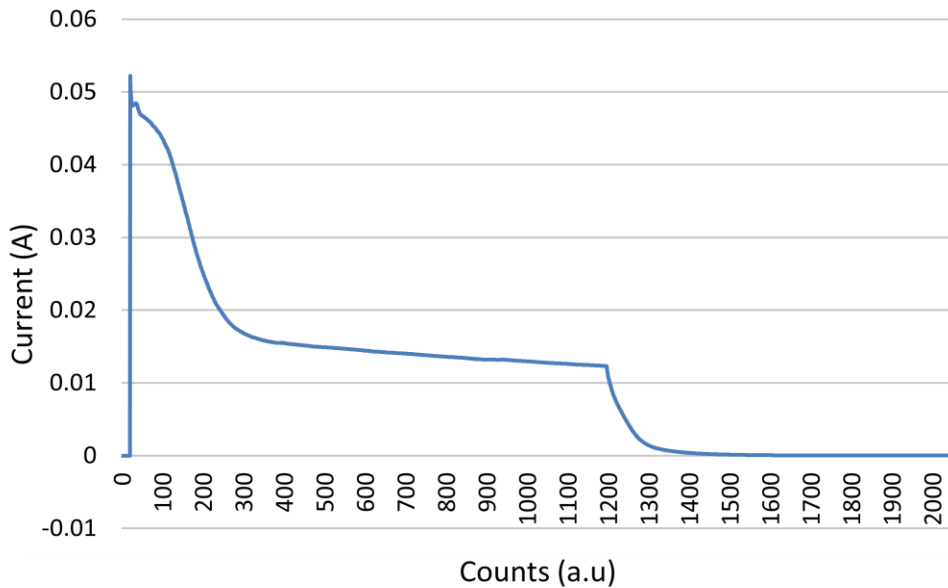


Figure 2.2: Current curve for TiO_2 anodization with a current compliance set at 0.05 A.

Upon analyzing the current curve, shown in Figure 2.2, that results from the electrochemical etch, there is a sharp increase in current followed by a slow decay. As the oxide layer forms on the surface of the titanium working electrode, the current decreases because of the insulating nature of the oxide. The curve then reaches a relatively constant current which is the result of ionic conduction within the electrolyte. Gas evolution is dominant in the earlier portion of the anodization and slows over time. This is an indication that electronic conduction is dominant in the first portion of the anodization because gas evolution requires electronic charge transfer to split H_2O to make O_2 gas. ^[11]

The nanotubes were annealed at high temperature in air to convert the amorphous TiO_2 into an anatase crystal structure. The parameters for the high temperature anneal are $25^\circ C$ to $400^\circ C$ over 3.5 h, $400^\circ C$ to $450^\circ C$ over 3 h, $450^\circ C$ to $25^\circ C$ over 3.5 h.

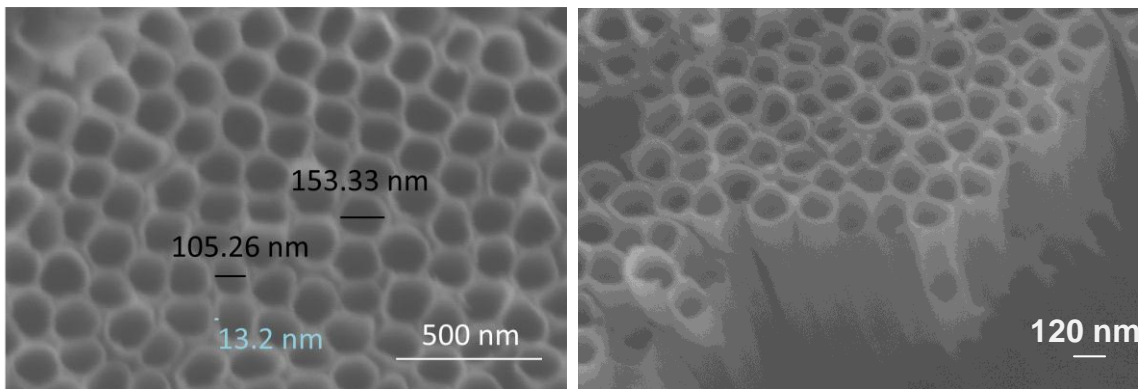


Figure 2.3: SEM image of top (left) and side (right) views of TiO_2 nanotubes. Dimensions for inner diameter (black) and wall thickness (blue) are given.

Once annealed, the nanotubes were imaged using Scanning Electron Microscopy (SEM). In this way, the structural characteristics are determined, including inner diameter and outer diameter of the tubes, uniformity of the tubes, existence of cracks, and other features. Figure 2.3 shows an SEM image taken of TiO₂ nanotubes. From these SEM images, the sizes of the nanotubes are found to be about 100 - 150 nm with wall thicknesses of 10-15 nm. The nanotubes are mostly uniform, but as can be seen in the image to the right, the areas with nanotube separation exhibit some breakage and cracking in the tubes, which commonly occur in the samples we have made.

2.1.2 Free-standing Nanotube Array Fabrication

Free-standing nanotube membrane fabrication has been a large focus in this project. The ability to remove the nanotubes from the substrate provides many avenues of research and new device architectures. By removing the nanotubes from the titanium substrate, other metals can be used to replace the titanium, the deposition of materials in open tubes may be much easier, and they can be used in semi-transparent device structures. Also, they could be used in flexible photovoltaic devices by infiltrating the nanotubes with suitable polymer materials.

Simple sonication or chemical removal of nanotube arrays have proven insufficient in achieving free-standing films. Either the nanotubes are not removed at all through these methods, or they were destroyed in the process. Chen and Xu ^[43] proposed a solution to this problem by anodizing a second time after annealing using a low

potential of 12 V over 3-8h. This second anodization etches the bottom barrier layer, creating a new amorphous TiO_2 barrier layer and releasing the nanotube membrane from the titanium substrate. Once removed, the nanotube membrane is immersed in a solution of 10 % H_2O_2 in water for 12 h to resolve the amorphous bottom layer. The overall process is depicted in Figure 2.4. The resulting free-standing nanotube array has an open top and bottom as seen in the SEM images, Figure 2.5.

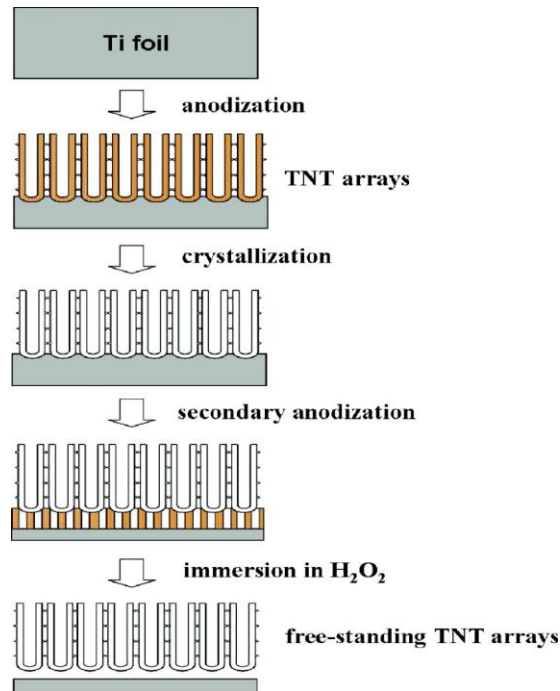


Figure 2.4: Method for fabricating free-standing nanotubes using a four step process. ^[45]

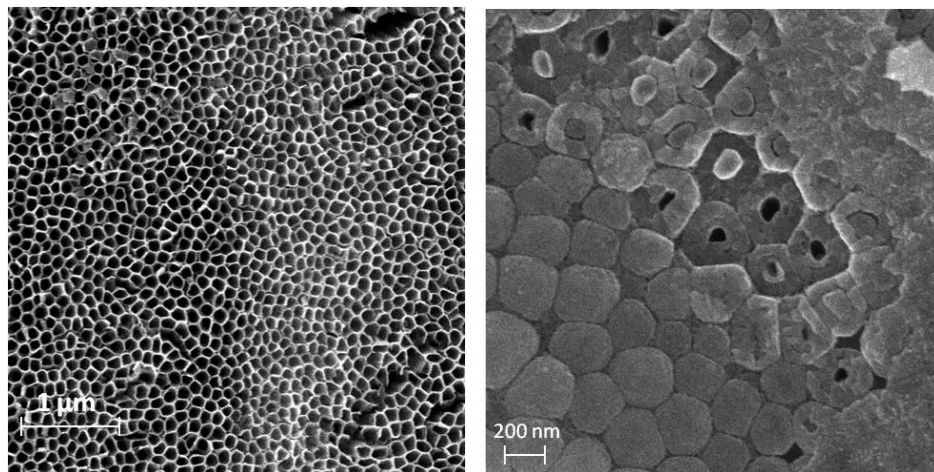


Figure 2.5: SEM images of a free-standing nanotube membrane from the top (left) and bottom (right) of the tubes.

We then took the removed nanotube array and demonstrated an application of a free-standing nanotube membrane. First, we took the fragile membrane and demonstrated the ability to deposit metals as a bottom electrode material through thermal evaporation. This replaces titanium, and allows more conductive metals to be used. An image of this membrane is given in Figure 2.6. The evaporator in our lab is no longer functioning, so this work was not continued although there is much promise in this area for further research.

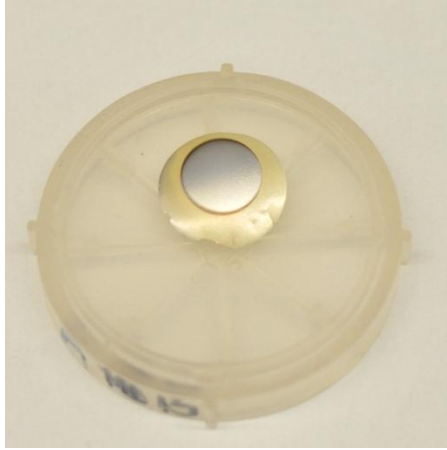


Figure 2.6: Image of a free-standing nanotube membrane with an aluminum electrode evaporated onto the bottom.

2.1.3 ZnO Fabrication

ZnO nanorods are fabricated through a two-step process consisting of the formation of a seed layer on the substrate followed by growth perpendicular to the substrate. ^[46] Cleaned ITO coated glass was used as the substrate for nanorod growth. A seed layer is first deposited on the substrate by spin-casting a solution of zinc acetate dehydrate (5mM) in ethanol at 2000 rpm for 30 seconds. This is repeated four times followed by baking at $\sim 250^{\circ}\text{C}$, which is just above the temperature required to convert zinc acetate into zinc oxide. The spin-cast and baking steps are repeated once. The substrate is then immersed in an aqueous solution of 0.1 M zinc nitrate hexahydrate and 0.1 M hexamethylenetetramine and heated in an oven at between $95\text{-}100^{\circ}\text{C}$ for 2 h at a slightly slanted, vertical angle ($\sim 70^{\circ}$ from the bottom). The residue is rinsed with DI water followed by drying with nitrogen gas.

The resulting nanorods have an orientation mostly perpendicular to the substrate with some deviation in direction, as seen in the SEM image provided in Figure 2.7. The nanorod diameters are between approximately 100-200 nm, showing a large amount of size variation.

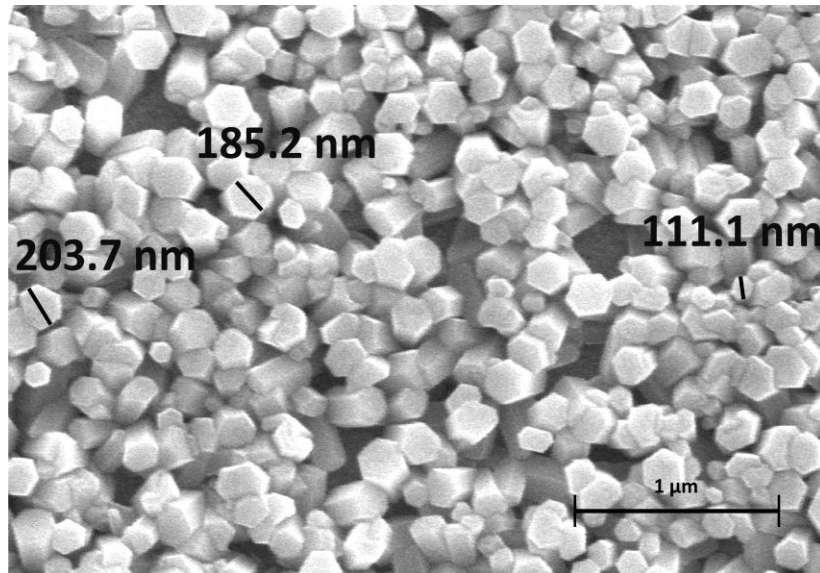


Figure 2.7: SEM image of ZnO nanorods grown on a seed layer.

2.2 Nanocrystal Synthesis and Modification

2.2.1 Nanocrystal Synthesis

CdSe nanocrystals are grown using 0.256 g CdO, 10 g trioctylphosphine oxide (TOPO), 10 g hexadecylamine (HDA), and 1.01 g dodecylphosphonic acid (DDPA) as precursor materials. This synthesis follows that of Bowers ^[47] with variation in the ratios

of starting materials and ODE was not used in this synthesis. The precursor materials are mixed in a three necked flask with a stir bar. A temperature probe is inserted in one of the openings on the side, while the other side is capped with a septum. A bump trap is fitted to the center. The precursor materials are heated while purging the flask with argon until 150°C is reached. At that point, the purge needle is removed from the septa. The temperature is allowed to rise to 330°C . The temperature is maintained at 330°C until the CdO is converted to cadmium phosphonate, at which point the solution should turn from a dark brown color to colorless. When the solution is colorless, Se: tributylphosphine (Se:TBP) is added. The addition of selenium starts the growth of the nanocrystals. The nanocrystals are allowed to grow until the appropriate size is reached, which is confirmed through absorption measurements. The solution is then cooled quickly with air flow until the temperature reaches approximately 90°C .

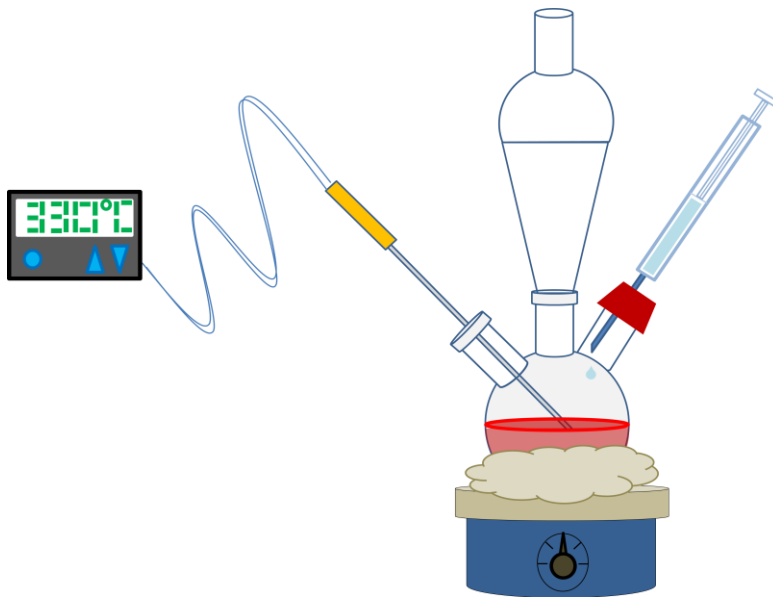


Figure 2.8: Nanocrystal synthesis apparatus including a temperature probe on the left, bump trap in the center, and a rubber septa on the right where injection occurs.

After synthesis, the nanocrystals are separated from the remaining precursor material and any other impurities through a cycle of precipitation and centrifugation steps. First, methanol is added to the nanocrystal solution to precipitate the nanocrystals. It is centrifuged at 6000 rpm for 15 minutes. After centrifugation, there should be a solid pellet at the bottom. The liquid is discarded, and the solid is allowed to dry for a short time. The solid is then redissolved in a small amount (~10 mL) of octanol and centrifuged at 6000 rpm for 30 minutes. The solid from this step is discarded and the liquid is kept. These steps are repeated as many times as is necessary to clean the nanocrystals. For our purposes, the methanol/octanol washes were only repeated once. After the final octanol step, there is one additional methanol wash to acquire a solid that can then be redissolved in the desired solvent. Toluene is used in most cases as a compatible solvent.

2.2.2 Ligand Exchange

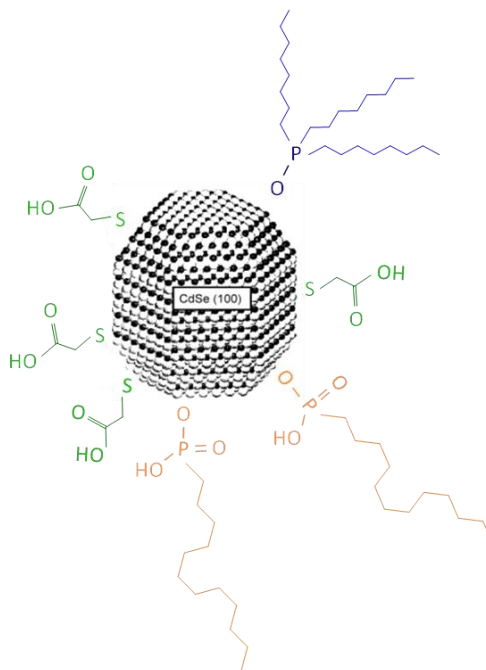


Figure 2.9: CdSe nanocrystal with MPA ligands exchanged onto a nanocrystal with as-synthesized ligands (TOPO and DDPA).

Ligand exchanges are done differently depending on the bond strength of the ligand on the nanocrystal compared to the replacement ligand. For most ligands with stronger bond strengths than the one that is being replaced, it can simply be added to the nanocrystal solution and the ligand exchange will occur almost immediately at room temperature. In the case of a ligand with low bond strength, the nanocrystal solution must be heated with the ligand in excess of the available metal bonding sites. As the ligands attach and detach from the nanocrystal, the quantity of bound ligands will be shifted toward the replacement ligand since its concentration is much higher in solution.

3-mercaptopropionic acid (MPA) binds almost immediately upon injection into the solution at room temperature. An example of an MPA bound CdSe nanocrystal is shown in Figure 2.9. Kamat *et al.* [25] used a stock solution of MPA in acetonitrile that was added to the nanocrystal solution in various concentrations in a study on its effect on nanocrystal emission. However, in most experiments, MPA can be added directly to the solution without pre-dilution. Once the exchange has occurred, the nanocrystals are no longer soluble in the organic solvent. It is centrifuged at 6000 rpm for 20 minutes. 1 mL of potassium tert-butoxide (1.0M in THF) and 2 mL N, N-dimethyl formamide (DMF) are added to the flocculant, which strips the proton from the carboxyl group on MPA. One final centrifuging step crashes out the nanocrystals so they can be redissolved in a polar solvent. The last step where potassium tert-butoxide and DMF are added may not be necessary in some cases. It is intended to make the nanocrystals water soluble, but this may not be necessary to attach the nanocrystal to TiO₂.

Pyridine is a weak-binding ligand, which can only be exchanged above room temperature. A small amount of pyridine is added to a vial of nanocrystals dissolved in an organic solvent. The ratio of pyridine to organic solvent must be low so that the nanocrystals can be centrifuged out after the exchange. This is the case only with pyridine, whereas other exchanges are done differently. The solution is heated to 90°C under stirring for 1 day. Hexanes is added to the solution, followed by centrifuging at 6000 rpm for 20 minutes. The nanocrystals are redissolved in a small amount of pyridine and heated again at 90°C under stirring for 1 day. Hexanes is added again, followed by centrifugation. The resulting nanocrystals should be significantly covered with pyridine, and are soluble in chloroform.

2.3 Deposition Methods

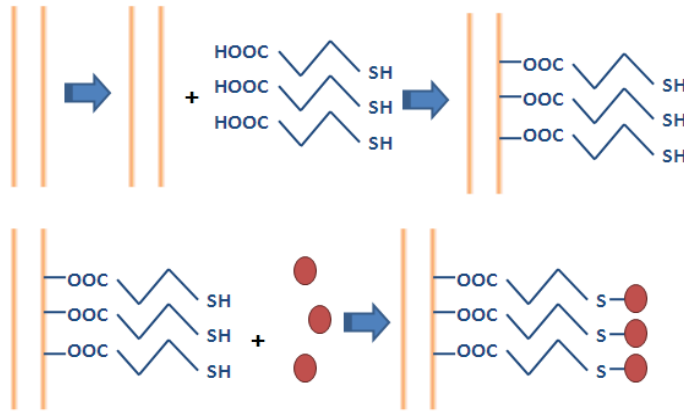


Figure 2.10: Illustration of chemical linking using a nanotube substrate (tan), MPA ligand (blue), and quantum dot (red). The quantum dot and TiO_2 nanotubes are chemically bonded through the linking molecule.

Nanocrystals can also be directly grown on a substrate through methods such as chemical bath deposition (CBD) ^[48, 49] or successive ionic layer adsorption and reaction (SILAR). ^[50] However, this limits the ability to choose the properties of the semiconductor nanocrystals, such as size and shape, as can be done with nanocrystals synthesized outside of the system that are then deposited. It also saves precursor materials when only the nanocrystals that become attached are used and the rest can be saved for another sample. This project focuses on nanocrystals that are introduced into the nanotube structure post-synthesis. This requires different coating methods such as immersion coating, electrophoretic deposition (EPD), and drop-casting.

2.3.1 Immersion Coating

Immersion coating can be used as long as a ligand on the nanocrystal will form a bond with the substrate. This method relies on the nanocrystals coming into contact with the substrate and locating a binding site. Since this is partially a diffusion process, it is time dependent. Essentially, the longer the substrate sits in solution, the more likely it is that it will be fully covered. Most of the samples were coated over 1-2 day time periods.

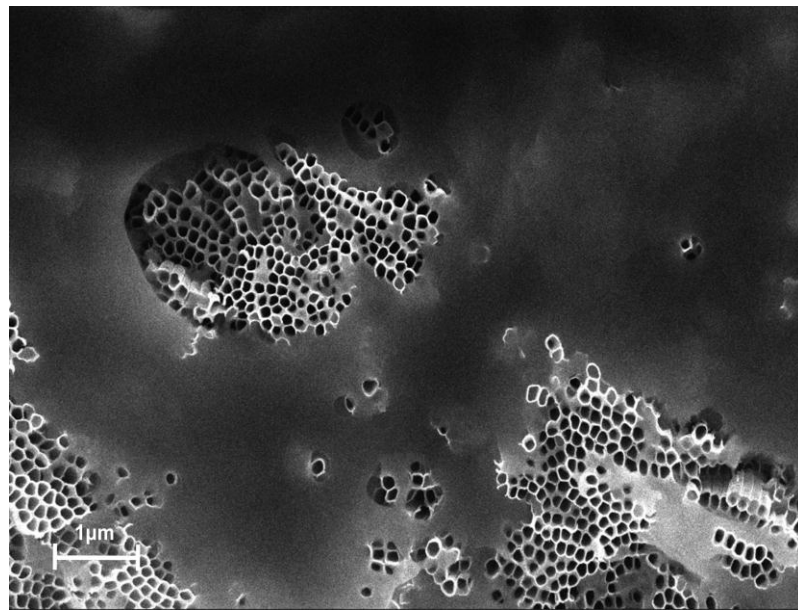


Figure 2.11: SEM image of nanocrystals aggregated at the surface of TiO₂ nanotubes.

Some factors must be considered when using this method, such as polarity of the substrate and nanocrystals, size of the nanocrystals in comparison to the tube diameter, and solvent effects. If the polarities are incompatible, aggregation will occur at the

surface of the tubes as seen in Figure 2.11. The size of the nanocrystals is less of a concern although it might become an issue if the nanotube diameter is smaller than 100 nm. In most cases, the nanocrystal will be significantly smaller than the nanotube diameter. Solvent effects may also play a role in the deposition. The ability of the solvent to wet the surface of the tubes properly has been considered in relation to deposition quality, but was not investigated in-depth.

2.3.2 Electrophoretic Deposition

Electrophoretic deposition (EPD) is a more convenient method of deposition due to its ability to deposit materials into thin films that may not covalently bind to the substrate as well as materials that do bind covalently. Studies ^[51-56] have been done with CdSe nanocrystals before ligand exchange, and it has been found that the nanocrystals will coat substrates despite the lack of covalent bonds.

We have performed EPD with MPA capped CdSe nanocrystals. MPA capped nanocrystals have already been used with other deposition methods. However, MPA has not been used to perform EPD. The advantage of ligand exchanging with MPA before EPD is to replace the insulating ligands, and also because a smaller potential is needed to deposit MPA coated nanocrystals. The method for ligand exchange has been explained previously. Once MPA capped nanocrystals are synthesized, a very dilute solution (< 0.05 optical density) is made. The substrate is immersed in the solution along with a counter-electrode placed parallel to each other. EPD was performed with a Keithley

2400 model sourcemeter as well as a Gelman Instrument Company 500 V power supply with similar results. A potential is applied, usually between 50-100 V over a short amount of time, 1-5 minutes.

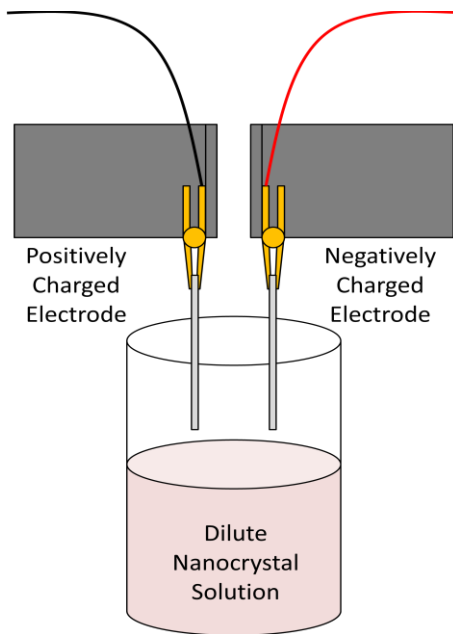


Figure 2.12: EPD setup with two electrodes spaced at a set distance and lowered into a dilute nanocrystal solution. The electrodes are connected to a Keithley 2400 sourcemeter.

Careful attention should be paid to the current as EPD is performed. With short-chain polar ligands, the current is significantly higher than with longer alkyl-chain lengths. According to literature,^[52-54] EPD is performed at 500 V for nanocrystals synthesized through a standard method^[55, 56] with insulating ligands. However, this potential must be reduced significantly with polar ligands due to the high current (above 150 mA) at 500 V, which was above the measurement limit for the power supply.

2.4 Device Preparation

2.4.1 Indium-Tin Oxide Electrode Modification

ITO coated glass slides are purchased from Delta Technologies, Limited with the following parameters. The dimensions are 25 x 25 x 1.1 mm. They are all SiO₂ passivated polished float glass with ITO coated on one side. When necessary, the ITO is patterned by masking the ITO surface with electrical tape, exposing the areas intended to be etched. The slide is then immersed in a 3 M HCl solution at 60 °C for approximately 15 minutes. After the exposed area is adequately etched, the slide is sonicated in isopropanol and acetone for 5 minutes each to clean the surface.

2.4.2 Polymer Deposition

After completing an anodization and annealing on a TiO₂ nanotube sample, nanocrystals are deposited using the methods mentioned above. Following nanocrystal deposition, tetraphenyl diaminobiphenyl (TPD) was spin-coated at 1000 rpm for 60 seconds. Then poly(3,4-ethylenedioxythiophene) poly(styrenesulfonate), referred to as PEDOT:PSS, was spin-coated two times at 2000 rpm for 60 seconds each. To promote further penetration within the pores and better contact, the sample is baked at 160 °C for 18 minutes. To complete the device, two layers of PEDOT:PSS were spin-coated onto the selectively etched ITO electrode at 2000 rpm for 60 seconds each. The electrode and

the nanotube substrate were sandwiched and baked together at 110 °C for 1 h. This completes the solid-state device.

2.4.3 Sealing the Electrolyte Device

The method of sealing the device is different depending on the device structure. In most cases, a thermoplastic sealant is used as a barrier between the electrodes as well as a reservoir for the electrolyte. In some cases, the sealant is cut so that there is an opening to inject the electrolyte solution. Small holes are cut in the sealant that allow for multiple testing areas to be incorporated onto one substrate in other device structures. The thermoplastic sealant is melted at 100 °C in an oven or on a hot plate. Careful attention must be paid to covering the exposed surfaces completely with the sealant so that electrical shorting can be prevented.

When testing larger areas, the sealant is cut in such a way that the electrolyte can be injected by capillary action into the spacing between the electrodes where the sealant is missing. The electrolyte can be regenerated by injecting more solution in as the liquid evaporates or leaks if necessary.

Chapter 3

Characterization Techniques for Solar Cell Materials

3.1 Scanning Electron Microscopy

SEM is a type of electron microscopy that is used to image surfaces in much the same way as an optical microscope with electrons replacing photons to image the surface. Photons have a longer wavelength than electrons, resulting in poor resolution as the sizes of particles become smaller. At the nanoscale, optical microscopes do not have adequate spatial resolution. SEM images surfaces by accelerating electrons at a target and measuring the interaction of those electrons with the target at a detector. For normal imaging purposes, a detector is installed to measure secondary electrons, and this is standard in most SEMs. However, most SEMs can be modified with other detectors as well for back-scattered electrons, characteristic X-rays, etc.

For our purposes, secondary electron measurement is used to image the surface of our nanostructures. The images produced are very high resolution, showing features as small as 1 to 5 nm depending on the quality of the microscope and the ability to create a high-vacuum sample chamber. Transmission electron microscopy is necessary for any features smaller than this size.

SEM can be a very useful tool when dealing with nanoscale technology. It is used extensively with nanotube and nanorod structures to show the length and diameter of the

structures. It is valuable for determining what problems may be limiting a device. Images of the nanotube structure can reveal cracks that may cause shorting, surface debris that may block the tube openings (Figure 3.1), and aggregation of nanocrystals at the base of the tubes (Figure 2.11). These problems can limit the efficiency of a device or possibly prevent it from acting as a working device altogether.

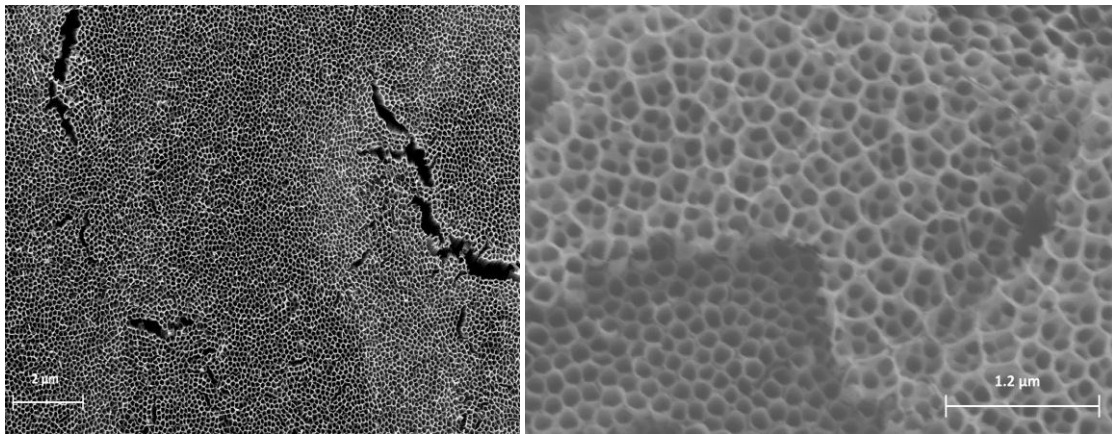


Figure 3.1: SEM images of TiO₂ nanotubes with cracks (left) and surface debris (right)

3.2 Rutherford Backscattering Spectroscopy (RBS)

RBS is an analytical technique used to determine the chemical composition and relative ratios of elements in a sample. High energy ions (He^{2+}) are accelerated toward a target, and backscattered ions are measured by a detector. The ions of a known energy hit the stationary sample and are elastically scattered back at the detector with an energy characteristic of the mass of the element being hit. He^{2+} ions are accelerated to an energy

of 1.8 MeV for our experiments at a backscattering angle, θ , equal to 176° , and the energy of the backscattered ion is plotted by counts per channel vs. channel number.

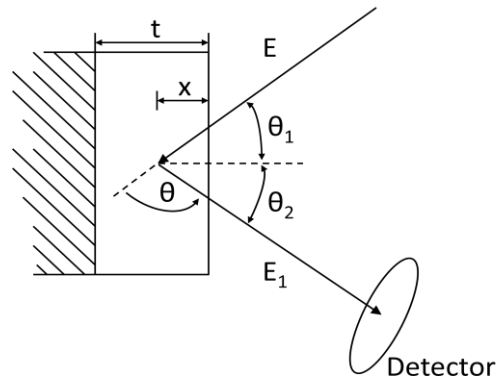


Figure 3.2: Diagram showing the laboratory angle θ , incident ion energy E , backscattered ion energy E_1 , distance the ion beam travels into the sample x , the sample thickness t , and the reflection angles of the ion beam θ_1 and θ_2 .

The RBS spectrum can be used to understand certain properties of the sample. Peak width gives an indication of how thick the film is due to decreasing energy as the incoming ions penetrate into the sample. The right-side peak edge represents the channel number associated with an element that shows peak fronting. In Figure 3.3, the count number for the large plateau on the left is labeled as E_2 . E_1 and E_3 are elements that have very small thickness on the substrate as is seen by the relative sharpness of the peaks.

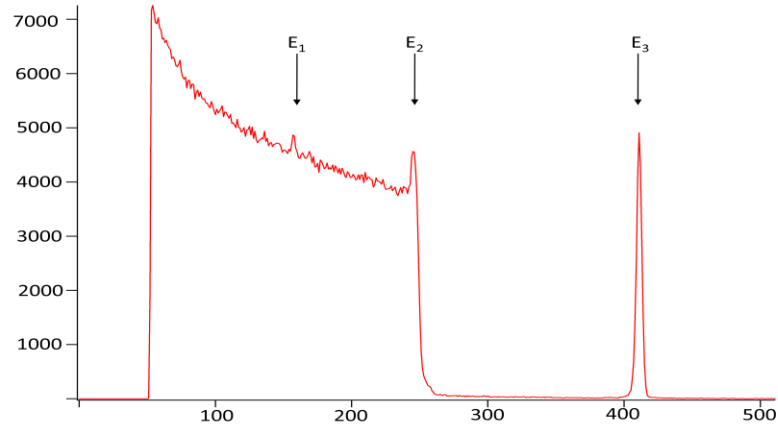


Figure 3.3: RBS spectrum of bismuth implanted silicon used as a standard for calculations. The energies of significant peaks are labeled E_1 , E_2 , and E_3 .

Unknown elements in a sample are determined by their kinematic factors, which are defined as the ratio of their backscattered ion energy to the initial ion energy or

$$K = E_{\text{backscattered}}/E_0 \quad (3.2.1)$$

where $E_{\text{backscattered}}$ is the backscattered ion energy, E_0 is the accelerated ion energy, and K is the kinematic factor

The K value is constant for any element and is used to identify elements by their isotopic mass and the angle θ . To identify unknowns directly from the counts per channel vs. channel number plot, it is important to consider that the channel number is logarithmically related to the backscattered ion energy. The backscattering energy goes to the square of the atomic number of the element of interest. However, it can be fit to a line to estimate the correct energy. This allows you to use the simple equation, $y = mx + b$, to solve for the energy of the unknown, then calculate the kinematic factor of an

element with that backscattered ion energy using equation 3.2.1. The following calculations are used to calculate K of an unknown element.

$$\text{Fit to a line: } E_{\text{backscattered}} = mx + b, \quad (3.2.2)$$

where m is the slope of the line, x is the channel number, and b is the y intercept.

$$\text{Calculate } E_{\text{backscattered}} \text{ for a known element: } E_{\text{backscattered}} = K * E_0, \quad (3.2.3)$$

using a known K and E_0 value.

$$\text{Calculate m using two known elements: } E_{C_d} - E_C = m (x_{C_d} - x_C) - 0, \quad (3.2.4)$$

E_{C_d} and E_C are the calculated energies from equation 3.2.3 and x_{C_d} and x_C are the channel numbers for those elements in the spectrum.

$$\text{Plug in known values to calculate b: } E_{C_d} = m * x_{C_d} + b, \quad (3.2.5)$$

$$\text{Solve for } E_{\text{unknown}}: E_{\text{unknown}} = m * x_{\text{unknown}} + b \quad (3.2.6)$$

where x_{unknown} is taken from the spectrum and m and b were calculated previously.

$$\text{Determine the K value for the unknown: } K = E_{\text{unknown}}/E_0 \quad (3.2.7)$$

Once all of the peaks have been identified, the stoichiometry of the elements can be identified by calculating the areal density, N_i , of each element and then comparing the ratio. When comparing two elements, A and B in the compound A_nB_m , the following equation describes the stoichiometric ratio.

$$\frac{n}{m} = \frac{N_A}{N_B} = \frac{A_B}{A_A} * \frac{\sigma_A(E,\theta)}{\sigma_B(E,\theta)} \quad (3.2.8)$$

The areal density is calculated using information gathered from the RBS spectra and known values from the experimental parameters. The following equations are used to calculate N_t ,

$$N_t = \frac{A_x * DTR * C_{Bi} * e}{Q_x * \Omega * \left(\frac{\sigma}{\sigma_R}\right)_x * \sigma_x(E, \theta)} \quad (3.2.9)$$

where some values are known and others are experimentally determined or calculated. Table 3.1 shows the variables that are used in this equation. The calculated values are determined by the following equations,

$$\sigma_x(E, \theta) = \frac{(\sigma_R)_x}{E_{lab}^2} * 10^{-24} \quad (3.2.10)$$

$$\left(\frac{\sigma}{\sigma_R}\right)_x = 1 - \left(\frac{0.49 * Z_1 Z_2^{4/3}}{E_{lab}}\right) \quad (3.2.11)$$

Equation 3.2.10 uses the known Rutherford cross sections at a set angle, θ , using the known lab energy, E_{lab} . This number must be corrected because the actual cross sections are not Rutherford at both high and low energies.

Experimental Parameters and Known Values		Calculated Values	
A_x	peak integration	Ω	solid angle of the detector
Q_x	integrated charge deposited on the sample	$\sigma_x(E, \theta)$	cross section at laboratory energy, E, through the angle θ .
DTR	dead-time-ratio	$\left(\frac{\sigma}{\sigma_R}\right)_x$	non-Rutherford correction factor
C_{Bi}	correction factor that gives correct N_{Bi} for bismuth standard		
e	elementary charge		
σ_R	Rutherford cross section		
Z_i	atomic number of the element of interest		
E_{lab}	incident laboratory kinetic energy of the analysis beam ions		
Table 3.1: Definition of constants and variables in the areal density calculation for RBS used to determine stoichiometric ratios of elements. ^[57]			

Once these values are known for both the bismuth standard and the sample being studied, they are used to solve for N_t of the element of interest. First, Ω must be solved for using equation 3.2.9 and a known areal density for the bismuth standard. When Ω is solved for, it is used in 3.2.9 to solve for N_t of a desired peak from the RBS spectrum.

Although more information can be acquired from RBS, knowledge of the above properties is sufficient for this project.

3.3 Solar Simulation Testing

Solar cells are tested using a 50 W Solux 4700K lamp that closely mimics the solar spectrum. Figure 3.4 shows the testing setup used for our devices. The setup consists of a metal box with a 3.9 cm diameter circular hole cut in the side to let light in with a rotating arm used to cover the hole for dark measurements. A metal lid is used to cover the top of the box during measurements in the dark. The interior of the box and lid is painted black to prevent light reflection that may affect efficiency measurements. The power meter, a Coherent Radiation Model 210 power meter, is situated such that the solar cell and the power meter are at the same distance from the light source when placed in front of the opening. The device is wired through a Keithley 2400 sourcemeter which is used to source a potential and measure the resulting current to acquire an IV curve. A LabView program written by Nat Smith is used to run the Keithley instrument and record the data. The data is then processed using data analysis software such as Igor Pro and Microsoft Excel.

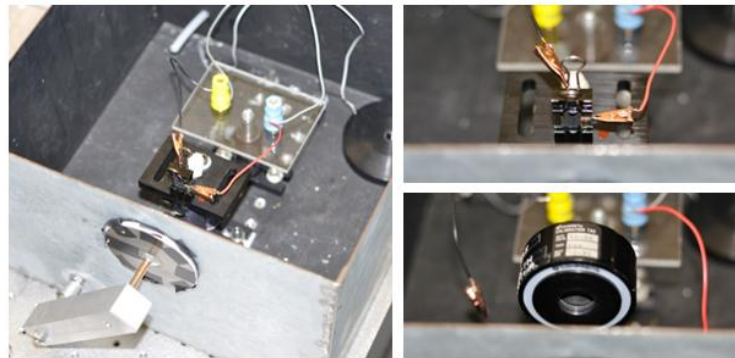


Figure 3.4: Lab setup for solar cell testing with a view of the device setup (top right), power meter setup (bottom right), and an overall view (left).

The first devices that were made and tested were nanotube-based solid-state solar cells with a TPD and PEDOT:PSS hole-conducting layer, as shown in 1.2. The IV curves for one of these devices are shown in Figure 3.5. The shape of the IV curves demonstrates proper device characteristics, as seen by an increase in current with increasing voltage with an area in the center that shows resistance to current flow from the materials in the device. However, there is no significant shift from dark to light in the region of interest. This indicates a very low efficiency although I later learned that a smaller voltage scan would be necessary to determine exactly what is occurring in that area. From previous research in this group by former members along with this data, it was determined that the efficiencies were far too low to publish. This led to a search for possible problems with our device design or measurement methods. Although our goal is an all-solid-state device architecture, I began to use a redox electrolyte to compare our devices to literature.

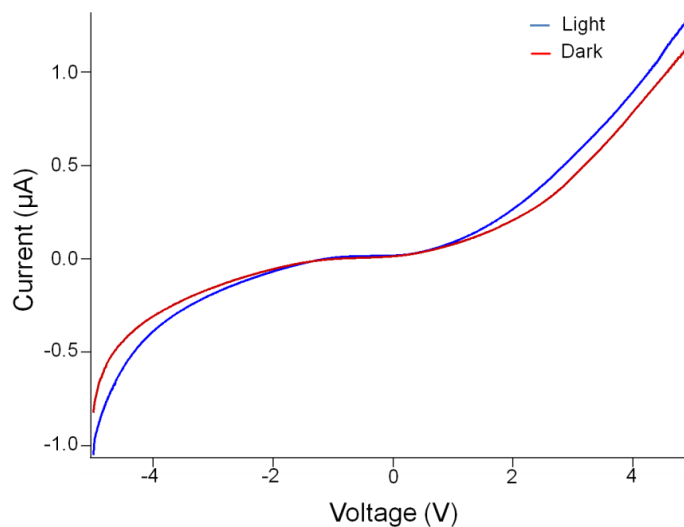


Figure 3.5: IV curve of a TiO_2 nanotube quantum dot-sensitized solar cell using a polymer hole-conducting layer. The efficiency and FF were not able to be calculated.

Initially, an iodine-based redox electrolyte was used because it was commonly used in solar cell architectures. The results of this attempt are given in Figure 3.6. A smaller voltage scan was used to measure this device to acquire more data points in the area of interest. The IV curve and power vs voltage curves are provided to show the activity in this region. The efficiency values of $6.01 \times 10^{-4} \%$ and $4.55 \times 10^{-4} \%$ were still very low. I soon found out that iodide electrolytes degrade CdSe nanocrystals, so it was replaced with a NaS electrolyte for further experiments although there was not much improvement.

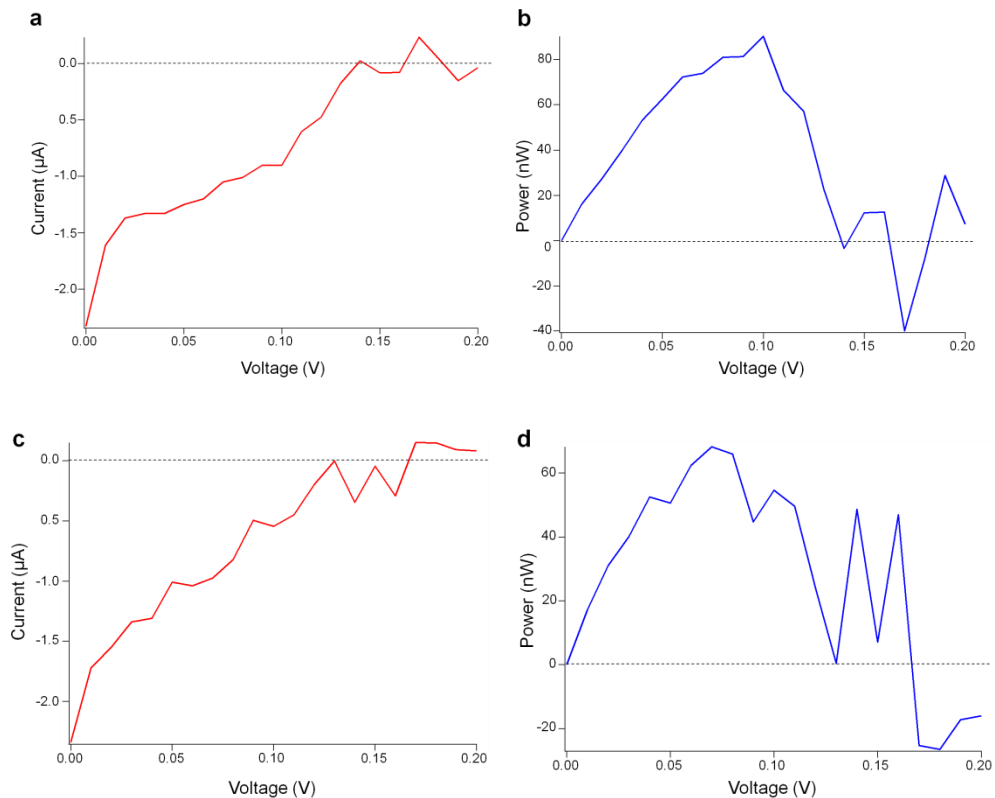


Figure 3.6: IV (a and c) and power vs voltage (b and d) curves of a TiO₂ nanotube quantum dot-sensitized solar cell using an iodine-based liquid electrolyte. The efficiency is $6.01 \times 10^{-4} \%$ (a) and $4.55 \times 10^{-4} \%$ (c). The FF is 0.29 (a) and 0.23 (c).

ZnO devices were also tested using a NaS electrolyte. The results of the solar simulation testing of a ZnO electrolyte-based quantum dot-sensitized solar cell are given in Figure 3.7. This device exhibited the expected shape of a working device and gave a useful curve in the area of interest, but it also had a poor efficiency like the other devices.

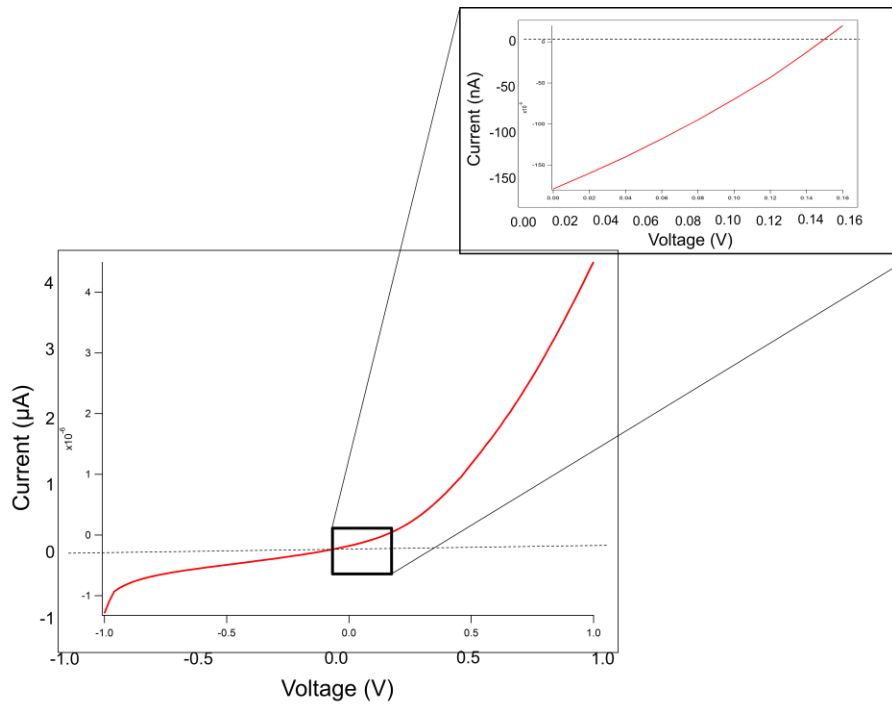


Figure 3.7: IV curve of a ZnO electrolyte-based quantum dot-sensitized solar cell with an efficiency of $7.45 \times 10^{-7} \%$ and a fill factor of 0.28. The area of interest is highlighted in the box.

Chapter 4

Conclusions and Future Directions

4.1 Conclusions

I have described in this thesis the fabrication and characterization of a quantum dot-sensitized solar cell. This device structure consists of a nanostructured electron transport substrate made of either TiO_2 or ZnO and semiconducting nanocrystals as light harvesters. For hole-conduction in the devices, a polymer solid-state device structure was used as well as a redox electrolyte.

This project has built upon the existing project prior to my work by accomplishing free-standing nanotube arrays allowing for flow-through deposition and attachment to more ideal substrates. I have demonstrated the ability to use this free-standing film to deposit nanocrystals and measure the absorbance by UV-Vis, giving the opportunity to quantify nanocrystal deposition which was not otherwise possible on the titanium substrate. There were difficulties in measuring adequate efficiencies, which I attribute to the lack of an adequate electrocatalytic counter-electrode in the devices where I used an electrolyte as well as poor deposition of the polymer hole-conducting material and nanocrystals in the solid-state solar cells. The next section will outline possible solutions to these issues for future research.

4.2 Future Directions

4.2.1 Graphene Counter-electrode

One of the problems mentioned earlier is the lack of an adequate electrocatalytic counter-electrode. Platinum is used as a catalyst in most published literature, but it is cost-prohibitive and not ideal for polysulfide electrolytes. Graphene^[58, 59] has become a material of great interest because of its extremely high conductivity and stability while being very cost-effective, renewable, and environmentally friendly. Graphite has already been used as an electrocatalytic material for photovoltaic devices,^[28] yet graphene is much more conductive than graphite^[60]. Due to these characteristics, it may be beneficial to use this as an electrode material. A study can be done to compare this to other known electrocatalytic materials to determine the viability of graphene in photovoltaics as an electrode.

4.2.2 Solid-state Photovoltaic Device using Free-standing Nanotubes

The solid-state device structure that this group has previously used in this project is flawed in one major aspect. The titanium substrate is bound to the nanotubes, preventing the use of other metals as electrodes. In addition to this problem, there is always an insulating barrier layer between the metal contact and the nanotube array. Removing the nanotube array allows for removal of the barrier layer and more choices of metal

contacts. A current problem with this device structure is attaching the nanotube membrane to a substrate. Once removed, the nanotube membrane is very brittle and difficult to handle. It also curls slightly, making attachment to a substrate problematic. It may be difficult at this point to make a device using this structure, but I believe research in this area is headed this direction.

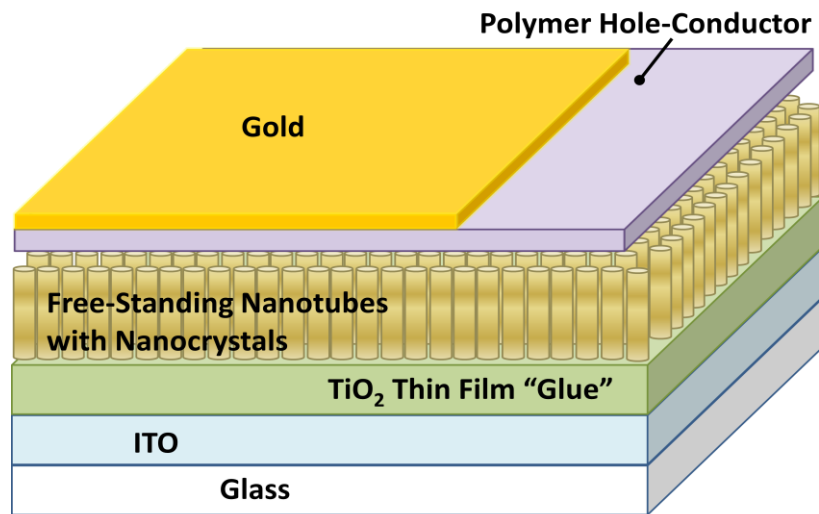


Figure 4.1: Device structure for a solid-state device using our previous structure with a removed nanotube membrane.

4.2.3 ZnO Solid-state Device

ZnO nanorods are a much easier platform for attaching nanocrystals and depositing a layer of hole-conducting material. As compared to nanotubes, nanorods are much easier to work with and require less processing. Further work in this area, such as optimizing the nanocrystal deposition, varying the hole-conducting material, and

substituting different nanocrystal materials provides many options for new research. ZnO is becoming a growing area of interest in photovoltaics.

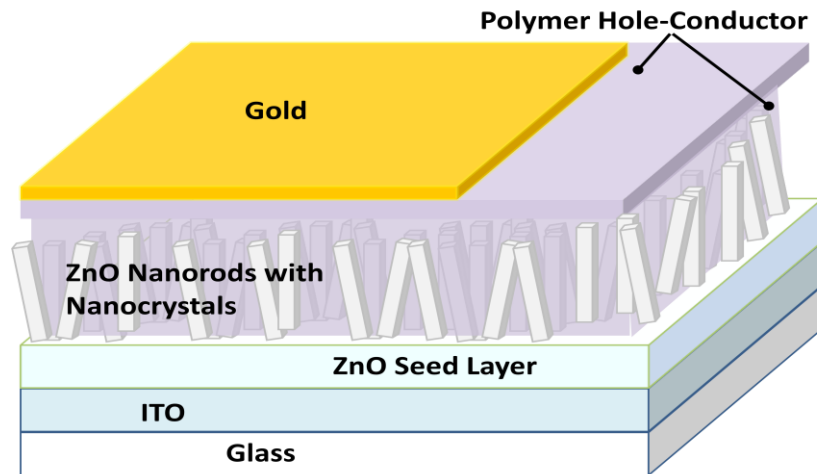


Figure 4.2: ZnO device structure for a solid-state solar cell

4.2.4 UV-Vis Study on Free-standing Nanotubes

As I mention in Appendix C, there is a possibility for further experiments to be done with free-standing nanotubes using UV-Vis. This is possible only for free-standing nanotubes and not for substrate-bound nanotubes, and it has not yet been done on TiO_2 nanotubes since the method for detaching the nanotubes was introduced in 2009. ^[44] This same type of experiment has been done for ZnO, ^[14] which is already translucent when fabricated.

Appendix A

Oak Ridge Ligand Exchange Experiment

A.1 Introduction

I have also been working on a side project through collaboration with Oak Ridge National Laboratory and University of Tennessee in Knoxville. This project involves exchanging the as-synthesized ligands on a nanocrystal with pyridine followed by a pyridine-functionalized hole-conducting polymer. Initial studies consisted of pyridine-functionalized polystyrene because attaching a pyridine group to polystyrene was much easier than for poly (3-hexylthiophene) P3HT, which is the more ideal polymer ligand for this project. RBS was used to characterize the nanocrystal samples before exchange and after pyridine and polymer exchange. The ligands used in this study are listed in the table below with the structure provided.

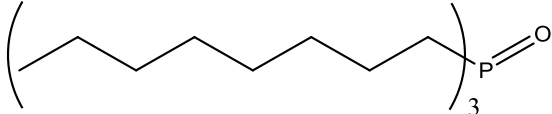
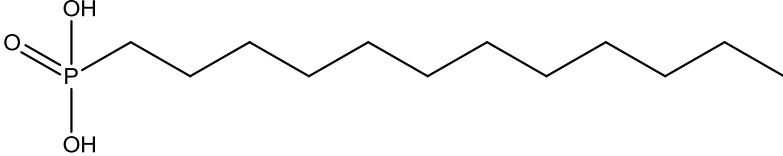
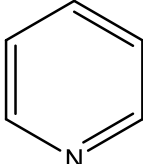
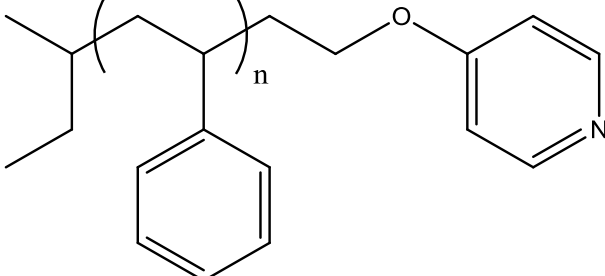
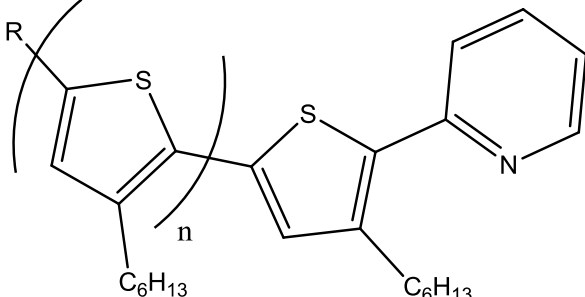
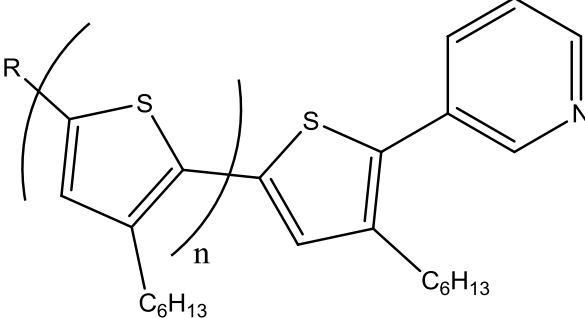
Name of Ligand	Ligand Structure
TOPO	
DDPA	
Pyridine	
Polystyrene (pyridine functionalized)	
P3HT (2- pyridine functionalized)	
P3HT (3- pyridine functionalized)	

Table A.1: List of ligand names and structures used in the ligand exchange study.

A.2 Ligand Exchange

Pyridine was exchanged with the as-synthesized ligands to take advantage of its low bond strength to the Cd on the nanocrystal surface. This makes it easier to exchange with the pyridine-functionalized polymers. Pyridine was exchanged on nanocrystals according to the method mentioned in section 2.2.2 with a few variations of duration and number of exchange cycles. In general, three cycles of diluting in pyridine, heating, centrifuging, and redissolving in pyridine were done over three to four days.

Following the pyridine exchange, the amount of polymer needed per Cd site on the nanocrystal was calculated so that a small excess could be added for exchange. The concentration is estimated by dividing the optical density by the molar absorptivity. The following equation is used to calculate the weight of polymer.

$$\text{mass}_{\text{Ligand}} = C_{\text{NC}} (V_{\text{NC}}) (\# \text{ Cd surface atoms}) (\text{MW}_{\text{Polymer}}) (N_{\text{A}}) \quad (\text{B2.1})$$

C_{NC} is the concentration of the nanocrystal solution, V_{NC} is the volume of that solution, $\text{MW}_{\text{Polymer}}$ is the molecular weight of the polymer, and N_{A} is Avogadro's number.

When the weight is determined, a slight increase in polymer is measured and added to the solution. The excess polymer ensures that every site has at least one polymer ligand to exchange for the pyridine ligand already attached to the Cd site. The polymer would be in excess of pyridine, so more polymer should bind than pyridine over time if the exchange is favorable.

The polymer exchange is done in chloroform since pyridine-capped nanocrystals are most soluble in chloroform. This creates a problem for increasing the temperature for exchange since the boiling point of chloroform is low, 61.2°C. To accommodate for the boiling point, the temperature of exchange was lowered to 40-50°C. It is allowed to equilibrate under heating for approximately one day.

A.3 Characterization

RBS is used to characterize the elemental composition of nanocrystal solutions and the stoichiometric ratio of those elements. It is ideal to have a ratio close to 1:1 of Cd:Se to ensure that no Cd precursor material is left in the solution, indicating that the wash cycles were adequate in cleaning the solution. One should look for the ratio of Cd to other unique elements in the ligands to signify a decrease or increase in ligand concentration on the nanocrystals. For pyridine exchange, nitrogen would be ideal to look for because an increase in nitrogen would indicate an exchange of pyridine for TOPO or DDPA. However, pyridine is easily removed under vacuum, so an increase in nitrogen would not be apparent using RBS. Therefore, a decrease in phosphorus and oxygen concentration would be needed to indicate a loss of TOPO and DDPA ligands, which would be replaced with pyridine.

When pyridine is replaced with pyridine-functionalized polystyrene or P3HT, there should be an evident nitrogen peak that will not be seen in the as-synthesized or pyridine exchanged samples. Also, a sulfur peak should appear in the P3HT capped

nanocrystals that will not be evident in the as-synthesized or pyridine capped nanocrystals.

Figure A.1 and A.2 show RBS spectra of a nanocrystal sample that was synthesized, then ligand exchanged with pyridine. The reduction in phosphorus and oxygen according to the areal density ratios, as determined by the stoichiometric ratio calculations shown in section 3.2, is characteristic of a replacement of TOPO and DDPA with pyridine. This is the expected result, which suggests that we achieved an exchange.

Further research in this area will be continued by another graduate student. The next step in this project is to perform an exchange with the other polymers and analyze the samples with RBS.

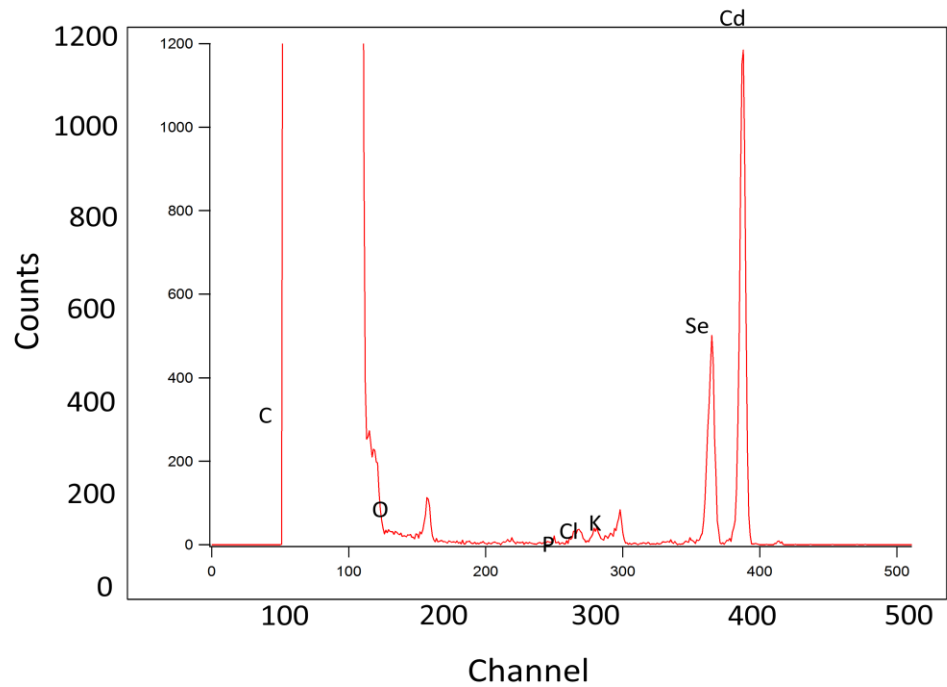


Figure A.1: CdSe nanocrystals in toluene synthesized through oleic acid synthesis.

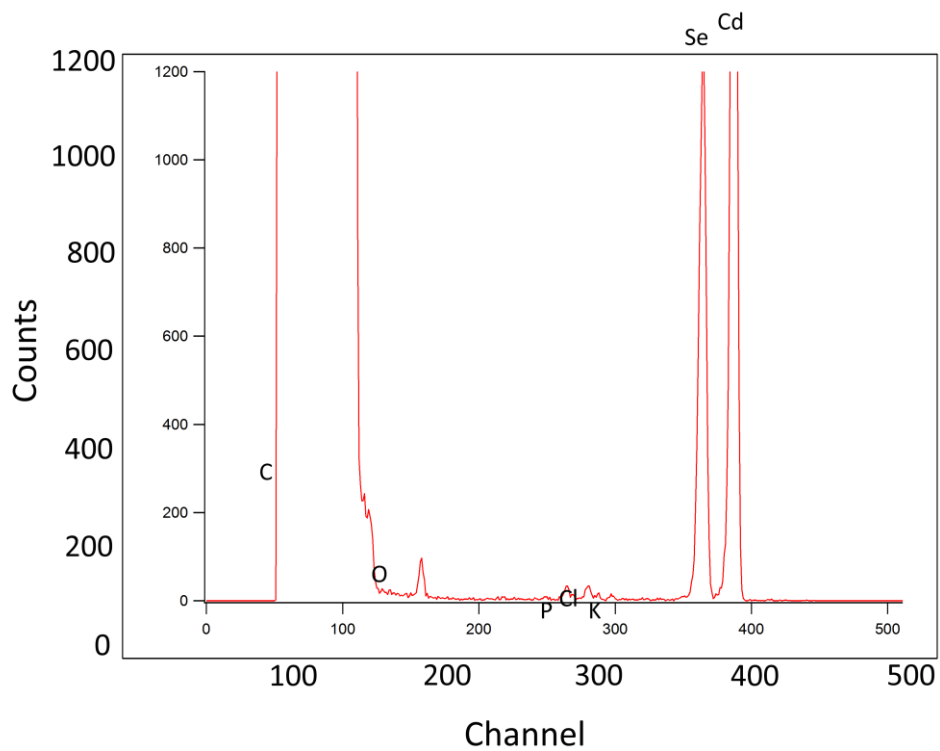


Figure A.2: CdSe nanocrystals in chloroform synthesized through oleic acid synthesis and ligand exchanged with pyridine.

Appendix B

TiO₂ Nanotube Imprinting

B.1 Introduction

In collaboration with Judson Rychman in Sharon Weiss's research group, I anodized TiO₂ nanotubes using standard methods as mentioned earlier followed by stamping with a silicon grating stamp ^[61] to form optical microstructures prepared by Judson. The silicon grating stamp was fabricated using standard contact lithography and reactive-ion etching techniques. The stamp was pressed against the substrate using a force of ~2000 N, creating parallel tracks in the nanotube array. The samples were then used in further studies which are on-going and not yet published.

B.2 Characterization

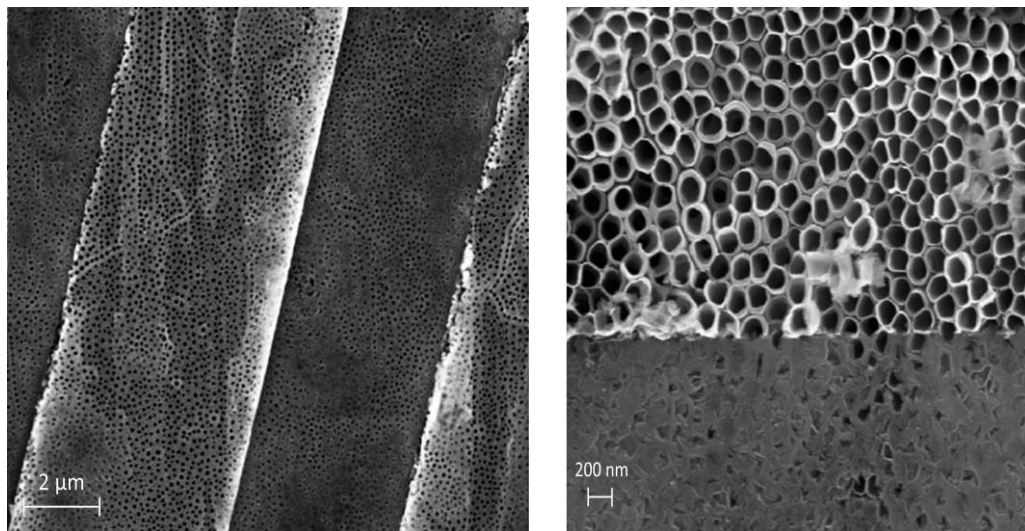


Figure B.1: Nanotube imprinting SEM images produced by Judson Rychman

Appendix C

Preliminary UV-Vis Study on Nanocrystal-coated Free-standing Nanotubes

C.1 Introduction

Removal of the nanotubes allows for a UV-Vis study to be done determining the nanocrystal concentration on the nanotubes. The titanium-bound nanotubes do not allow light to pass through; after removal, the nanotube membrane is translucent and allows for a study to be done quantifying nanocrystal deposition using differing methods. A preliminary UV-Vis experiment was done to show that it is possible to do this, as shown in Figure C.1. There is a lot of noise in the spectra due to scattering from the nanotube membrane. However, there is a clear absorbance increase as a result of nanocrystal deposition on the nanotubes. It is possible to estimate nanocrystal concentration on the nanotubes using this method. This study is not completed, and is included in future work.

C.2 Characterization

In Figure C.1, the nanotube baseline is at approximately 0.0 absorbance intensity at 550 nm, where the nanocrystal absorbance peak is found. The optical density of the nanotubes is approximately 1.0 after nanocrystals are added. Using the absorbance wavelength of the nanocrystal and the optical density increase, the concentration of nanocrystals can be estimated. With an optical density of 1.0 and a nanocrystal

absorbance at 550 nm, the concentration can be estimated to be 8.9×10^{-6} M. This is calculated using the Beer-Lambert law, solved for concentration:

$$C_{\text{NC}} = \frac{A}{\epsilon * b} \quad (\text{C.1})$$

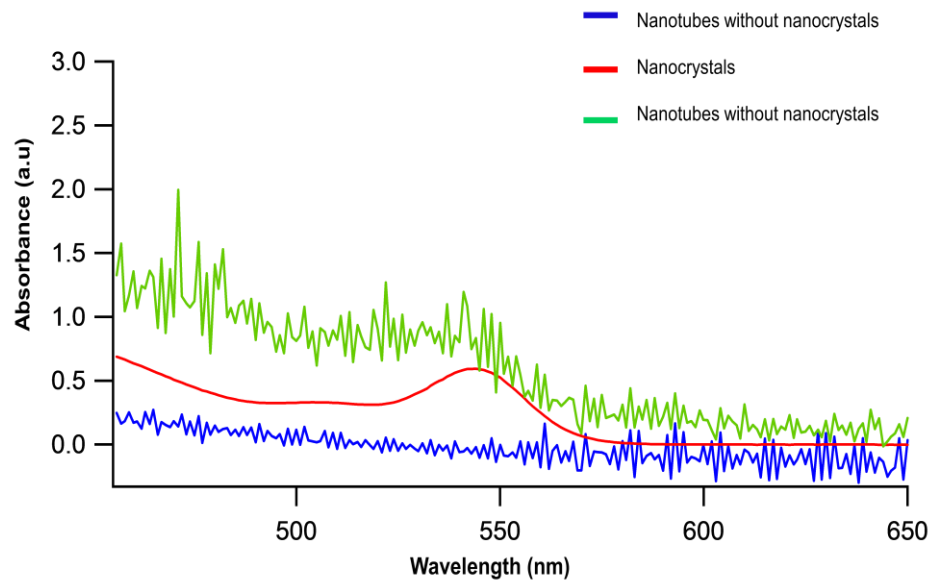


Figure C.1: UV-Vis spectrum of nanotubes, nanocrystals, and nanotubes + nanocrystals

REFERENCES

1. Becquerel AE. *Comptes Rendus*. **1839**, 9, 561–567.
2. Jenny Nelson; *The Physics of Solar Cells*. London, UK: Imperial College Press, 2003; pp 1-16.
3. Chapin DM, Fuller CS, Pearson GL. *J. Appl. Phys.* **1954**, 25, 676-677.
4. Green MA, Ho- Baillie A. *Prog. Photovoltaics*. **2010**, 18, 42-47.
5. Oregan B, Grätzel M. *Nature*. **1991**, 353, 737-740.
6. Greenham NC, Peng X, Alivisatos AP. *Phys. Rev. B*. **1996**, 54, 17628.
7. Shankar K, Mor GK, Prakasam HE, Yoriya S, Paulose M, Varghese OK, Grimes CA. *Nanotechnology* **2007**, 18, 065707.
8. Mor GK, Varghese OK, Paulose M, Mukherjee N, Grimes CA. *J Mater Res*. **2003**, 18, 2588-2593.
9. Prakasam HE, Shankar K, Paulose M, Varghese OK, Grimes CA. *J. Phys. Chem. C*. **2007**, 111, 7235-7241.
10. Mor GK, Varghese OK, Paulose M, Grimes CA. *Adv. Funct. Mater.* **2003**, 15, 1291-1296.
11. Varghese OK, Paulose M, Gong D, Grimes CA, Dickey EC. *J. Mater. Res*. **2003**, 18, 156.

12. Pascaul J, Camassel H, Mathieu H. *Physical Review Letters*. **1977**, *39*, 1490-1493.
13. Zang Z, Shi YY, Sun XL, Cao HT, Lu HM, Liu XD. *Materials Research Bulletin*. **2010**, *45*, 474-480.
14. Leschkies KS, Divakar R, Basu J, Enache-Pommer E, Norris DJ, and Aydil ES. *Nano Lett.* **2007**, *7*, 1793-1798.
15. Kamat PV. *J. Phys. Chem. C*. **2008**, *112*, 18737-18753.
16. Gregg BA. *J. Phys. Chem. B*. **2003**, *107*, 4688.
17. Schmelz, O.; Mews, A.; Basche', T.; Herrmann, A.; Mu'llen, K. *Langmuir* **2001**, *17*, 2861-2865.
18. Moreels I, Lambert K, de Muynck D, Vanhaecke F, Poelman D, Martins JC, Allan G, Hens Zeger. *Chem. Mater.* **2007**, *19*, 6101–6106.
19. Gao F, Wang Y, Shi D, Zhang J, Wang M, Jing X, Humphry-Baker R, Wang P, Zakeeruddin SM, Grätzel M. *J. Am. Chem. Soc.* **2008**, *130*, 10720–10728.
20. Chamarro M, Gourdon C, Lavallard P, Lublinskaya O, Ekimov AI. *Nuovo Cimento D*. **1995**, *17*, 1407-1412.
21. Kongkanand A, Tvrđy K, Takechi K, Kuno M, Kamat PV. *J. Am. Chem. Soc.* **2008**, *130*, 4007-4015.
22. Reference Solar Spectral Irradiance: ASTM G-173.
<http://rredc.nrel.gov/solar/spectra/am1.5/ASTMG173/ASTMG173.html>. (accessed on November 05 2010).

23. Marcus RA. *J. Chem. Phys.* **1956**, *24*, 966-978.
24. Marcus RA, Sutin N. *Biochim Biophys Acta.* **1985**, *811*, 265-322.
25. Bakkers EPAM, Roest AL, Marsman AW, Jennekens JW, de Jong-van Steensel LI, Kelly JJ, Vanmaekelbergh D. *J. Phys. Chem. B.* **2000**, *104*, 7266-7272.
26. Baker DR, Kamat PV. *Langmuir.* **2010**, *23*, 11272-11276.
27. Koole R, Schapotschnikow P, Donega CD, Vlugt TJH, Meijerink A. *ACS Nano.* **2008**, *2*, 1703-1714.
28. Puzder A, Williamson AJ, Zaitseva N, Galli G, Manna L, Alivisatos AP. *Nano Lett.* **2004**, *4*, 2361-2365.
29. Wuister SF, Donega CD, Meijerink A. *J. Phys. Chem. B.* **2004**, *108*, 17393-17397.
30. Robel I, Subramanian V, Kuno M, Kamat PV. *J. Am. Chem. Soc.* **2006**, *128*, 2385-2393.
31. Mora-Seró I, Giménez S, Moehl T, Fabregat-Santiago F, Lana- Villareal T, Gómez R, Bisquert J. *Nanotechnology.* **2008**, *19*, 424007.
32. Ahmad S, Yum JH, Butt HJ, Nazeeruddin MK, Grätzel. *Chemphyschem.* **2010**, *11*, 2814-2819.
33. Grätzel M. *Nature.* **2001**, *414*, 338-344.
34. Liu CJ, Olsen J, Sounders DR, Wang JH. *J. Electrochem. Soc.* **1981**, *128*, 1224.

35. Ueno Y, Minoura H, Nishikawa T, Masayasu T. *J. Electrochem. Soc.* **1983**, *130*, 43.
36. Bang JH, Kamat PV. *ACS Nano.* **2009**, *3*, 1467-1476.
37. Licht S, Khaselev O, Ramakrishnan PA, Soga T, Umeno M. *J. Phys. Chem. B.* **1998**, *102*, 2536.
38. Hodes G, Manassen J, Cahen D. *J. Electrochem. Soc.* **1980**, *127*, 544.
39. Heremans P, Cheyns D, Rand BP. *Accounts Chem. Res.* **2009**, *42*, 1740-1747.
40. Leschkies KS, Jacobs AG, Norris DJ, Aydil ES. *Appl. Phys. Lett.* **2009**, *95*, 193103.
41. Mihailetschi VD, Blom PWM, Hummelen JC, Rispens MT. *J. Appl. Phys.* **2003**, *94*, 6849-6854.
42. Liu J, Shi Y, Yang Y, *Adv. Funct. Mater.* **2001**, *11*, 420.
43. Standard Testing Conditions (STC) in the Photovoltaic (PV) Industry.
http://www.imtsolar.com/public/files/IMT%20Solar_STC%20for%20PV%20APP%20N%20OTE.pdf. (accessed on September 29, 2010). IMT Solar.
44. Albu SP, Ghicov A, Aldabergenova S, Dreschsel P, LeClere D, Thompson GE, Macak JM, Schmuki P. *Adv. Mater.* **2008**, *20*, 4135.
45. Chen Q, Xu D. *J. Phys. Chem. C.* **2009**, *113*, 6310-6314.
46. Yang LL, Zhao QX, Willander M. *J. Alloy Compd.* **2009**, *469*, 623-629.
47. Bowers MJ, McBride JR, Rosenthal SJ. *J. Am. Chem. Soc.* **2005**, *127*, 15378-15379.

48. Niitsoo O, Sarkar SK, Pejoux C, Rühle S, Cahen D, Hodes G. *J. Photochem. Photobiol.* **2006**, *181*, 306-311.
49. Diguna LJ, Shen Q, Kobayashi J, Toyoda T. *Appl. Phys. Lett.* **2007**, *91*, 023116.
50. Lee HJ, Wang M, Chen P, Gamelin DR, Zakeeruddin SM, Grätzel M, Nazeeruddin MK. *Nano Lett.* **2009**, *9*, 4221-4227.
51. Ueno Y, Minoura H, Nishikawa T, Masayasu T. *J. Electrochem. Soc.* **1983**, *130*, 43.
52. Hasan SA, Kavich DW, Mahajan SV, Dickerson JH. *Thin Solid Films.* **2009**, *517*, 2665-2669.
53. Smith NJ, Emmitt KJ, Rosenthal SJ. *Appl. Phys. Lett.* **2008**, *93*, 043504.
54. Jia SG, Banerjee S, Lee D, Bevk J, Kysar JW, Herman IP. *J. Appl. Phys.* **2009**, *105*, 103513.
55. Peng ZA, Peng XG. *J. Am. Chem. Soc.* **2001**, *123*, 183.
56. Rosenthal SJ, McBride JR, Pennycook SJ, and Feldman LC. *Surf. Sci. Rep.* **2007**, *62*, 111
57. Tesmer JR and Nastasi M. *Handbook of Modern Ion Beam Materials Analysis*. Pittsburg, PA, USA: Materials Research Society, 1995; pp 39-74.
58. Novoselov KS, Geim AK, Morozov SV, Jiang D, Zhang Y, Dubonos SV, Grigorieva IV, Firsov AA. *Science.* **2004**, *306*, 666-669.
59. Juang ZY, Wu CY, Lu AY, Su CY, Leou KC, Chen FR, Tsai CH. *Carbon.* **2010**, *48*, 3169-3174.

60. Meyyappan, M. *Carbon Nanotubes: Science and Applications*. CRC Press, 2005; p 289.

61. Ryckman JD, Liscidini M, Sipe JE, Weiss SM. *Appl. Phys. Lett.* **2010**, 96, 171103.